Southern Hemispheric Westerlies control sedimentary processes of Laguna Azul (south-eastern Patagonia, Argentina)

Bernd Zolitschka,[1] Michael Fey,[1] Stephanie Janssen,[2] Nora I Maidana,[3] Christoph Mayr,[4,5] Sabine Wulf,[6,7] Torsten Haberzettl,[8] Hugo Corbella,[9] Andreas Lücke,[10] Christian Ohlendorf[1] and Frank Schäbitz[2]

[1]University of Bremen, Institute of Geography, Germany

[2]

[2]University of Cologne, Institute of Geography and Education, Germany

[3]Universidad Nacional de Buenos Aires – CONICET, Argentina

[4]Ludwig-Maximilians-Universität München, GeoBio-Center^{LMU} and Department of Geo- and Environmental Sciences, Germany

[5]Friedrich-Alexander-Universität Erlangen-Nürnberg, Institute of Geography, Germany

[6]GFZ German Research Centre for Geosciences, Potsdam, Germany

[7]University of Portsmouth, Department of Geography, UK

[8]University of Greifswald, Institute of Geography and Geology, Germany

[9]Museo Argentino de Ciencias Naturales Bernardino Rivadavia, Buenos Aires, Argentina

[10]Forschungszentrum Jülich GmbH, Institute of Bio- and Geosciences, IBG-3: Agrosphere, Germany

Corresponding author:

Bernd Zolitschka, University of Bremen, Institute of Geography, GEOPOLAR, Celsiusstr. 2, D-28359 Bremen, Germany.

Email: zoli@uni-bremen.de

Abstract

Multiproxy investigations of lacustrine sediments from Laguna Azul (52 °S) document multi-millennial Holocene influences of Southern Hemispheric Westerlies (SHW) on the hydroclimatic variability of southeastern Patagonia. During the last 4000 years, this hydroclimatic variability is overprinted by centennial warm/dry periods. A cool/wet period from 11,600–10,100 cal. BP is succeeded by an Early Holocene dry period (10,100–8300 cal. BP) with a shallow lake, strong anoxia, methanogenesis and high salinity. Between 8300 and 4000 cal. BP the influence of SHW weakened, resulting in a freshwater lake considered to be related to less arid conditions. Since 4000 cal. BP, regional temperature decreased accompanied by re-intensification of SHW reaching full strength since 3000 cal. BP. Centred around 2200, 1000 cal. BP and in the 20th century, Laguna Azul experienced century-long warm/dry spells. Between these dry periods, two pronounced moist periods are suggested to be contemporaneous to the "Dark Age Cold Period" and the "Little Ice Age". Different from millennial SHW variations, centennial fluctuations appear to be synchronous for South America and the Northern Hemisphere. Changes in solar activity, large volcanic eruptions and/or modulations of ocean circulation are potential triggers for this synchronicity.

Keywords

XRF scanning, tephra layers, lake-level fluctuations, ectogenic meromixis, salinity changes, Holocene climate change, Roman Climate Anomaly (RCA), Dark Age Cold Period (DACP), Medieval Climate Anomaly (MCA), Little Ice Age (LIA)

Introduction

The intensity and latitudinal position of Southern Hemispheric Westerlies (SHW) are fundamental for global carbon cycling. A more southern position causes degassing of CO_2 from the deep ocean to the atmosphere whereas a more northern position decreases ocean-water ventilation resulting in additional atmospheric CO_2 transfer to intermediate water levels (Lovenduski et al., 2008). Today, southward shifting and intensifying winds are increasingly reducing the efficiency of the Southern Ocean as a carbon sink (Le Quere et al., 2007; Lovenduski et al., 2015). This influences the rate of CO_2 accumulation in the atmosphere (Fischer et al., 2010), modifies the natural greenhouse effect and causes droughts on Southern Hemispheric continents (Fletcher and Moreno, 2012). Aside from natural climate variability (Jones and Widmann, 2004), this is related to a mid-latitude temperature increase (Shindell and Schmidt, 2004) and reduced ozone concentration across Antarctica (Kang et al., 2011). Today, SHW are responsible for more than 25 % of the interannual global atmospheric CO_2 flux variability (Takahashi et al., 2012). Therefore, it is important to understand the mechanisms that drive SHW and explain their response to global climate change (Toggweiler et al., 2006).

Against this background we investigate a sediment record from Laguna Azul in southeastern Patagonia. This lake without surficial inflow and outflow is highly sensitive to hydroclimatic shifts and strongly dependent on the precipitation/evaporation ratio, which in turn affects aquatic biota and lacustrine geochemistry (cf., Schindler, 2009). Such lakes typically respond rapidly to environmental variability with changes in lake levels, redox conditions and salinity (Valero-Garces et al., 1996).

A first study of sediments from Laguna Azul focused on the last millennium and recognized a temporal equivalent of the Northern Hemispheric “Medieval Climate

Anomaly" (MCA) and the "Little Ice Age" (LIA) as well as recent anthropogenic disturbances (Mayr et al., 2005). In the same region it was demonstrated for Laguna Potrok Aike that wind-related evaporation is a controlling factor of its hydrological balance (Mayr et al., 2007a; Ohlendorf et al., 2013). Overall, regional environmental variations are linked to SHW, the dominant atmospheric circulation pattern in these latitudes (Garreaud et al., 2013; Toggweiler et al., 2006). SHW are controlled by insolation with complex feedbacks to the ocean-atmosphere-cryosphere system. Negative (positive) correlations between zonal wind and the amount of precipitation are documented for eastern (western) Patagonia (Garreaud et al., 2013; Moreno et al., 2014). Thus, rainfall decreases with intensified SHW east of the Andes and increases west of the Andes. Moreover, strong SHW prevent moist Atlantic low-pressure systems from entering the continent amplifying aridity in eastern Patagonia (Garreaud et al., 2013; Mayr et al., 2007b). In Argentina, droughts reduce the amount of rainfall and thus the availability of water for drinking, agriculture, industry and hydropower production causing socio-economic damage (Berman et al., 2012). Nowadays, permanently strong SHW with little precipitation are one cause for desertification and wind erosion in arid regions of southeastern Patagonia. Therefore, understanding SHW variability and its forcing provides information to deal with future climate change scenarios in this part of South America.

Despite its importance, little knowledge exists about past SHW variations. Available studies often provide controversial conclusions (Fletcher and Moreno, 2012; Kilian and Lamy, 2012; Moreno et al., 2014) due to different sensitivities of SHW recording, different suitability of proxies for SHW reconstruction and differences jn temporal resolution with associated chronological issues. Moreover, it is likely that reconstructions relying on precipitation-related proxies like pollen-based vegetation changes (e.g., Moreno and Videla, 2016) or runoff changes related to minerogenic sediment transfer (e.g., Lamy et al., 2010) are much less pronounced in semiarid eastern Patagonia compared to west of the Andes, because the amount of rainfall is lower by a factor exceeding 10 east of the Andes (Garreaud et al., 2013). In any case, interpretation of paleoenvironmental data in relation to zonal wind fields is not straightforward and involves a chain of assumptions (Kohfeld et al., 2013).

Here we present a high-resolution multiproxy study to assess intensity and position of the SHW throughout the Holocene. Furthermore, we compare our findings with regional hydroclimatic fluctuations to gain a better understanding of past and future climate changes.

Site description

Laguna Azul, a crater lake of the Pliocene to Late Quaternary Pali Aike Volcanic Field (D'Orazio et al., 2000), is one of the few permanent lakes in the semiarid steppe of extra-Andean southeastern Patagonia (52°04.7’ S, 69°35’ W, 100 m asl; Fig. 1). Its rugged morphology and the well-preserved pyroclastic ring wall point to a young monogenetic volcanic system (cf., Nemeth and Kereszturi, 2015) supported by $^{40}Ar/^{39}Ar$ ages (0.01 ±0.02 Ma) of a related lava flow (Corbella, 2002).

The lake is elliptical in shape (560 m x 240 m; Fig. 1) and exhibits overlapping sub-basins with a maximum water depth of 56 m in 2003. Lake shores consist of basaltic rocks except in the west where sand and lapilli-sized pyroclastics prevail. The catchment area (0.24 km^2) is restricted to the inner crater walls and is small in relation to the modern lake surface area (0.15 km^2). Laguna Azul is dimictic, holomictic and groundwater-fed without tributaries or outlets (Zolitschka et al., 2006). Continuous logging of limnological parameters from March 2002 to February 2005 reveals a stratified water body with a well-developed metalimnion from 17–25 m water depth during southern summers. The lake is classified as mesotrophic to eutrophic with epilimnetic pH values between 8.5 and 9.0, mean electric conductivity of 443 µS cm^{-1} and salinity of 0.3 ‰ (Mayr et al., 2005; Messyasz et al., 2007; Zolitschka et al., 2006).

Laguna Azul is situated in the dry Magellanic grass steppe (León et al., 1998). Nearest stands of subantarctic deciduous forests, dominated by southern beech (*Nothofagus pumilio* and *N. antarctica*), occur along the eastern foothills of the Andes about 160 km to the west. The climate of southeastern Patagonia is dominated by westerly winds and a rain-shadow east of the Andes. Correlation fields between local precipitation and zonal wind speed document a low (c. -0.3; Garreaud et al., 2013) to high (c. -0.8; Moreno et al., 2014) negative correlation for the study site. In addition, the weather station at Laguna Potrok Aike (~60 km west of Laguna Azul) shows that precipitation event frequency is dominated by westerly winds. However, occasional events from the east provide very high rainfall (Mayr et al., 2007b). Altogether, these factors result in a cool-temperate semidesert climate with extremely windy and highly evaporative conditions (Garreaud et al., 2013). At Laguna Azul the sum of annual precipitation is in the range of 200–300 mm with a mean annual temperature of 6–7 °C (Oliva et al., 2001).

Material and methods

Sediment coring and subsampling

The record is composed of overlapping cores recovered in the lake centre (52° 04.77’ S, 69° 34.83’ W) at 51 m water depth in February 2003 (Fig. 1). Sediment cores AZU 03/4 and AZU 03/6 were obtained with a UWITEC piston-corer (liner length: 5 m, inner diameter: 60 mm). The upper 40 cm of the 754 cm-long composite record are derived from gravity core AZU 03/5 in order to obtain an undisturbed sediment/water interface. The composite profile was established by macroscopic correlation supported by magnetic susceptibility (Fig. S1).

After recovery, sediment cores were sealed gas-tight, transported to the University of Bremen (Germany) and stored cool and dark. Cores were split lengthwise, photographed and lithologically described. After employing non-destructive logging techniques, cores were subsampled volumetrically in contiguous 1 cm intervals. Aliquots from each subsample were split for multiproxy analyses (Ohlendorf et al., 2011) carried out at 1 cm resolution except for stable isotopes and pollen (both 4 cm), biogenic silica (8 cm) and diatoms (16 cm).

Dating

Nineteen AMS ^{14}C samples were dated at the Poznań Radiocarbon Laboratory, Poland. Of the fifteen samples from the composite profile and two from the gravity cores AZU 02/4 and AZU 02/11 (Fig. 1), only four contained wood or terrestrial plant remains. Therefore, dating was extended to aquatic material (Tab. 1). Additionally, a sample of aquatic macrophytes was obtained from lake sediments exposed 2 m above the present lake level (Fig. 1). To test for a potential reservoir effect living aquatic macrophytes were also dated (Mayr et al., 2005).

An age-depth model was constructed with the R package clam 2.2 (Blaauw, 2010). All ^{14}C-ages were calibrated with the Southern Hemisphere calibration curve SHCal13 (Hogg et al., 2013) and the post-bomb calibration curve SH1–2 for postmodern ^{14}C dates (Hua et al., 2013). The sediment/water interface (AD 2003) was used as additional tie point. For age modelling the smoothed spline option (type = 4 with spar 0.3) of clam 2.2 was applied to the 13 radiocarbon ages between dashed lines in Tab. 1. Beyond the oldest dating point ages were extrapolated. All calibrated and modelled radiocarbon ages were rounded to decadal values.

Two macroscopically visible volcanic ash (tephra) layers were analysed petrographically and geochemically (cf. supplementary material for more information).

Geochemistry

Relative changes of element counts were obtained from the split core surface with 1 cm spatial resolution using a CORTEX X-ray fluorescence (XRF) core scanner (Croudace and Rothwell, 2015; Zolitschka et al., 2001) at the IODP Bremen Core Repository (MARUM, University of Bremen). Thirteen elements were measured of which five (K, Ca, Mn, Fe, Ti) were used for interpretation. Normalization of XRF data was achieved by dividing respective elements by Ti, an element related to minerogenic matter.

Total carbon (TC), total nitrogen (TN) and total sulphur (TS) were measured with a CNS elemental analyser (EuroEA, Eurovector). Prior to measurements, freeze-dried subsamples were ground and homogenized after removing plant macro remains. Concentrations of total organic carbon (TOC) were determined after treatment with 3 and 20 % HCl at 80 °C to remove carbonates. To distinguish TOC of autochthonous from allochthonous sources, C/N ratios were calculated as TOC/TN_{molar}. Total inorganic carbon (TIC) was determined as difference between TC and TOC. Calcium carbonate percentages (carb) were calculated by multiplying TIC values with the stoichiometric factor 8.33. To emphasize low-frequency variabilities, selected elemental data are plotted as seven-point running means (7PRM).

Biogenic silica (BSi) was analysed with the conventional automated leaching method (Müller and Schneider, 1993) and by applying a less time-consuming pressure pulping method with alkaline digestion in autoclaves (cf. supplementary material for more information). The amount of biogenic matter (BioM) is estimated as the sum of BSi and TOC, for the latter using the conversion factor of 2.13 (Dean, 1974).

Physical properties and mineralogy

Dry bulk density (DBD) was calculated from the weights of fresh and freeze-dried volumetric subsamples. Volume specific magnetic susceptibility (MS) was measured on split cores in 1 cm increments with a Bartington MS2E sensor employed on an automated measuring bench (Dearing, 1994; Nowaczyk, 2001). Additionally, the contribution of minerogenic matter (MM) is estimated as the difference between 100 % and the sum of biogenic matter (BioM) and carbonates (carb). The mineralogical composition of selected samples was determined by standard powder X-ray diffraction (XRD) with a Philips X'Pert Pro MD equipped with an X'Celerator Detector Array at the Geosciences Department (University of Bremen, Germany).

Stable isotopes

Subsamples for isotopic analyses were freeze-dried, homogenized with a spatula and sieved (200 µm) to eliminate macro remains. Nitrogen stable isotope ratios ($\delta^{15}N$) were determined on bulk sediment weighed into tin capsules and combusted at 1080 °C in an elemental analyser (EuroEA, Eurovector) with automated sample supply linked to an isotope-ratio-mass spectrometer (Isoprime, Micromass). For analyses of stable isotope ratios of organic carbon ($\delta^{13}C_{org}$) samples were decalcified with HCl (5 %) for 6 h in a water bath at 50 °C to remove calcite and siderite, centrifuged, rinsed repeatedly with deionized water to neutral pH and freeze-dried. Organic carbon-isotope ratios were determined using a Carlo Erba elemental analyser linked to an Optima isotope-ratio mass-spectrometer or with the system described above for nitrogen isotope-analyses. Isotope ratios are reported as δ values in per mil according to the equation

$$\delta = (R_s/R_{st} - 1) * 1000,$$

where R_s and R_{st} are the isotope ratios ($^{13}C/^{12}C$, $^{15}N/^{14}N$) of the samples and international standards (VPDB for carbon, AIR for nitrogen). Analytical uncertainty (1 σ) is 0.14 ‰ for $\delta^{15}N$ and 0.08 ‰ for $\delta^{13}C_{org}$.

Pollen and diatoms

Pollen samples were processed according to standard techniques (Faegri and Iversen, 1989). Pollen percentages of *Nothofagus-dombeyi*-type (including *N. pumilio* and *N. antarctica*) were calculated from pollen sums excluding aquatic taxa and spores. Additionally, Poaceae pollen sums were calculated excluding all wind-transported Andean forest taxa (AFT), their major representative at Laguna Azul is *Nothofagus-dombeyi*-type pollen*.* This was necessary because inclusion of AFT in the pollen sum would have influenced pollen percentages of the Magellanic steppe taxa, an effect not related to changes of the steppe vegetation surrounding Laguna Azul. Pollen counts in each pollen sample ranged from 260–550 grains depending on the presence of AFT. Reference collections and specific literature (Heusser, 1971; Markgraf and D'Antoni, 1978) were used for identification.

Diatom samples were prepared following standard procedures (Battarbee, 1986). A minimum of 400 valves were counted to calculate relative frequencies. Identification is based on standard literature (e.g., Krammer and Lange-Bertalot, 1986; Krammer and Lange-Bertalot, 1988; Krammer and Lange-Bertalot, 1991a; Krammer and Lange-Bertalot, 1991b; Rumrich et al., 2000; Simonsen, 1987).

Multivariate statistics

Unconstrained cluster analysis CONISS (Grimm, 1987) was applied to selected minerogenic (DBD, MS, TIC, Fe/Mn, Ca/Ti) and organic (TOC, TOC/TN, TS) parameters to characterize sediment composition and to obtain lithological zones.

Results and interpretation of the multiproxy record

Lithology

Based on CONISS, the record from Laguna Azul is subdivided into five lithological units (A–E; Figs. 2, S3). Basal unit A (754–728 cm) consists of graded basaltic scoria with grain sizes ranging from volcanic gravel up to ~1 cm in diameter to coarse ash. Because of the minerogenic composition of unit A, analyses were not carried out for pollen, diatoms and stable isotopes. Compared to minerogenic unit A (1.6 % BioM), the other units have distinctly higher contents of BioM (15.8–82.7 %) and classify as diatomaceous ooze (Tab. S2). Organic sediments start with unit B (728–686 cm; 15.8 % mean BioM) characterized as dark grey biogenic sediment with intercalations of dark and light layers. Unit C (686–641 cm; 37.7 % BioM) is black and laminated while unit D (641–588 cm; 42.7 % BioM) is characterized by fine laminations changing in colour from dark olive and black to dark grey. The uppermost highly organic lithological unit E (588–0 cm; 65.2 % BioM) makes up 79 % of the entire record and consists of reddish-brown to brown and faintly layered to homogenous diatomaceous ooze. CONISS separates it into four subunits (Ea–Ed). Lowermost subunit Ea (588–563 cm; 40.9 % BioM) contains two visible volcanic ash layers between 586 and 580 cm (Fig. S2) and the first of two dark grey to black layers with intercalated coarse sand grains labelled as sandy layer S1 (568–563 cm). The succeeding subunit Eb (563–466 cm; 62.8 % BioM) ends after the second sandy layer (S2; 476.5–474.5 cm) followed by subunits Ec (466–201 cm; 74.2 % BioM) and Ed (201–0 cm; 82.7 % BioM; Fig. 2).

Minerogenic sediment components

For minerogenic unit A, the elements Ti and Ca as well as MS and DBD show the highest values of the record. Compositionally, they correspond to the alkali-basaltic bedrock. At the base of lithological unit B, Ti is high (230 cps), then decreases to ~100 cps and finally increases again to 260 cps (Fig. 5). The mean value of Ti for unit B is 157 cps. A distinct drop in Ti marks the transition to unit C (mean: 97 cps). At the start of unit D Ti increases to 210 cps. One peak reaches >300 cps but the mean for unit D is 149 cps. From unit D towards the top of the profile Ti steadily decreases to 35 cps. Sandy layers S1 and S2 interrupt this trend with higher values (Figs. 2, 3).

Total inorganic carbon (TIC) summarizes different carbonate minerals, e.g. calcite, rhodochrosite and siderite. The variability of this proxy is similar for units B–D. At the beginning of each unit, TIC values increase to >0.5 % (labelled TIC1–TIC3 in Fig. 3) and thereafter diminish to <0.2 %. This pattern changes to a higher frequency (TIC4–TIC10) throughout unit E (Fig. 3). Two of these maxima (TIC4, TIC7) coincide with sandy layers S1 and S2. The last three maxima (TIC8–TIC10) reach higher values of up to 0.9 wt. % TIC (Fig. 3).

Compared to TIC, the Ca/Ti ratio is rather constant along units B–D with values around 2 (Fig. 3). TIC1 is not evident from this parameter, while TIC2 and TIC3 are weakly represented. Subunit Ea has low Ca/Ti ratios, except for both tephra layers. Subunit Eb separates in two parts: a lower half with values <2 and little variability and a variable upper half (values >4). Sandy layers are not manifested by this parameter.

Potassium is associated with silicates and regarded as additional proxy for minerogenic sediment. However, K/Ti shows constant low values throughout the record with three exceptions: both tephra layers and a less pronounced peak in unit C (Fig. 3). As K is not a major component of basaltic rocks (cf., low values in unit A and for both sandy layers), it is attributed to precipitation from the water column and thus not a proxy for allochthonous minerogenic sediment.

The elements Fe and Mn display a different pattern compared to proxies for minerogenic components. Both are redox-sensitive and regarded as transitional between minerogenic and organic records in lacustrine sediments (Fig. 3). The Fe/Mn ratio is indicative for reducing conditions in lake sediments. Increasing Fe/Mn links to more prominent anoxia and can be applied as a palaeo-redox indicator (Haberzettl et al., 2007). During early lithological units B and C the Fe/Mn ratio peaks and decreases thereafter (Fig. 3, Tab. S2). From unit D to subunit Eb it is stable at low values. However, two peaks interrupt subunits Ea and Eb linked to sandy layers S1 and S2. With the onset of subunit Ec the Fe/Mn ratio increases to a maximum and then decreases towards subunit Ed.

Due to the highly organic character of the lacustrine deposits, XRD analyses detected only few minerals (Tab. S3): quartz and plagioclase are present in units C–Ea, pyrite in units B–C, vivianite in unit D and calcite in unit Ec.

Organic sediment components

TOC comprises autochthonous and allochthonous organic matter. Lithological unit B has rather low and almost constant values (mean: 2.3 %). A distinct increase to a mean of 5.5 % characterizes unit C. From the onset of unit D, TOC constantly increases towards 16 % at the top of subunit Eb (Fig. 4, Tab. S2). Subunit Ea has three and subunit Eb one excursion to lower values linked to tephras and sandy layers (Figs. 2, 4). Finally, TOC drops to 12 % at the onset of subunit Ec and increases again to 15 % in topmost subunit Ed.

A general trend towards higher lacustrine productivity with time (Tab. S2) is documented by TOC and confirmed by BSi. Both parameters correlate positively (r=0.87, n=96). BSi documents opal mainly from diatoms. Like TOC, BSi values drop for sandy and tephra layers. However, volcanic ash layers are veiled in our BSi record due to its lower resolution.

Total sulphur in lake sediments is bound to the authigenic mineral pyrite (FeS) formed under anoxic conditions in the presence of iron. The TS record (Fig. 4, Tab. S2) shows 1.9 % for unit B and increases distinctly to 4.5 % in unit C. Units D–E are uniform with much lower values (0.4–0.6 %). TS is positively correlated with Fe/Ti (r=0.75, n=736). At the transition from subunit Eb to Ec two peaks >1.5 % TS occur. The older is contemporaneous to sandy layer S2 (Fig. 4).

Chronology and age-depth model

Calibrated radiocarbon ages range from 30,460 ±660 to -15 ±5 cal. BP (Tab. 1). To a sediment depth of 640 cm (modelled age: 8220 +120/-290 cal. BP), 13 radiocarbon ages consistently increase with depth. From 727–644 cm four dates between 19,460 ±320 and 30,460 ±660 cal. BP show age reversals and are much older than their stratigraphic position suggests (Tab. 1).

The sample of modern *Potamogeton* reveals a post-modern value (104.9 pMC) and post-bomb calibration results in probability ranges with two mean ages: -31 ±28 and -35 ±27 cal. BP. The aquatic macrophyte sample from the raised lake-level terrace provides an age range from 1290–1090 cal. BP (Mayr et al., 2005) (Fig. 1, Tab. 1).

The four radiocarbon dates much older than 8050 cal. BP have not been included in our chronology. Hard-water effects can be excluded as indicated by the date from the modern aquatic plant. Furthermore, carbonates are absent from the catchment area. Thus, reservoir effects linked to reworked organic material and juvenile volcanic CO_2 remain to explain the unexpected old and reversed radiocarbon ages. There is additional evidence for a younger sediment age from the continuous regional pollen curve of *Nothofagus*, which started to spread in the Southern Andes with Lateglacial warming (Recasens et al., 2012; Wille et al., 2007). As the *Nothofagus* pollen record at Laguna Azul reached a value of 40.5 % at the bottom of unit B (Fig. 4), this points to a maximum age of less than 15,000 cal. BP for the lacustrine record in agreement with the date of the lava flow.

Therefore, the age-depth model is based in lithological unit D at 8220 +120/-290 cal. BP (Tab. 1; Fig. 2). For greater depths, the constant sedimentation rate of Unit D (0.25 mm yr^{-1}) was extrapolated. This assumption most likely is imprecise because distinct lithological changes usually relate to changes in sedimentation rates. Regardless of these limitations, we assigned an age of 11,790 +390/-720 cal. BP to the onset of lacustrine deposits (Tab. S2). The radiocarbon-based mean sedimentation rate of the entire lacustrine record is 0.62 mm yr^{-1} with highest values (2.35 mm yr^{-1}) for subunit Ec and lowest sedimentation rates (0.25 mm yr^{-1}) for units B–D (Fig. 2, Tab. S2).

The sediment record from Laguna Azul contains two macroscopic tephra layers (Fig. S2). Details of their interpretation are documented in the supplementary material. Additional time control was expected from tephrochronology, as many dated volcanic ash layers have been documented for South America (Del Carlo et al., 2018; Fontijn et al., 2014; Fontijn et al., 2016; Wastegard et al., 2013). However, while this data contributes to the Patagonian tephrostratigraphy, it provides no additional information to improve the chronology of our record, which entirely relies on radiocarbon dating.

Volcanic signal

We interpret the basaltic scoria that compose unit A as redeposition of volcaniclastic material during the early lake stage immediately after volcanic activities have ceased (cf., Pirrung et al., 2008). This allows estimating the age of volcanic eruptions at Laguna Azul more precisely. While the $^{40}Ar/^{39}Ar$ age of 0.01 ±0.02 Ma (Corbella, 2002) is rather imprecise, we now can provide a Lateglacial minimum age of 11,790 +390/-720 cal. BP as extrapolated for the onset of unit B (Fig. 2).

Further evidence of young volcanism at Laguna Azul is distinguishable from the four lowermost radiocarbon ages that appear >9000 years too old (Tab. 1). Excluding reworked terrestrial organic matter, the most plausible explanation for this phenomenon is post-volcanic emission of juvenile CO_2 leading to a pronounced volcanic reservoir effect. An age overestimation of 500–800 years was noticed at the base of sediments from an overgrown Holocene crater lake on the South Atlantic island of Tristan da Cunha (Ljung et al., 2006). Up to 4400 years have been documented for modern samples from the Azores (Pasquier-Cardin et al., 1999) and up to 9500 years for Lateglacial aquatic samples from crater-lake sediments of Lago Grande di Monticchio, Italy (Hajdas et al., 1998).

Pollen evidence

The pollen record is dominated by *Nothofagus* and Poaceae (Mayr et al., 2007b; Schäbitz et al., 2013). While Poaceae constitute the most important element of local Magellanic steppe vegetation, trees of southern beech (*Nothofagus)* never grew in this region. Therefore, *Nothofagus* pollen grains recorded at our site represent long-distance transport by strong westerly winds (Gassmann and Pérez, 2006; Wille et al., 2007) and are regarded as supraregional indicators of SHW intensity (Mayr et al., 2007b). Throughout the entire record, *Nothofagus* values range from 18.0–37.5 %

while Poaceae (percentages calculated outside the AFT sum*)* vary from 56.6–70.9 % (Fig. 4, Tab. S2).

Interpreted as a SHW proxy, *Nothofagus* pollen maxima (minima) are related to stronger (weaker) westerly winds. Based on the negative correlation between SHW and rainfall for southeastern Patagonia (Garreaud et al., 2013; Moreno et al., 2014), we conclude that three more arid and two less arid periods occurred (Fig. 4). At the Early Holocene onset of lacustrine deposition, *Nothofagus* pollen samples reach >33 % indicating windier conditions with higher evapotranspiration resulting in a negative water balance. After this dry phase, *Nothofagus* pollen amounts fell to mean values of 26.2 % in unit B until 10,100 cal. BP indicating a less arid period. Unit C is characterized by *Nothofagus* pollen values reaching 33.1 % interpreted as pronounced dry phase from 10,100–8300 cal. BP. From 8300–3000 cal. BP (units D–Eb) *Nothofagus* pollen amounts decreased reaching minima of 20.5–18.5 % during subunits Ea and Eb (Fig. 4, Tab. S2) indicating the second less windy and less arid period. Around 3000 cal. BP *Nothofagus* pollen amounts increased again with maxima of >40 % documenting stronger aridity.

However, for the period AD 1460–1740 cal. BP Poaceae pollen amounts increased to a mean of 64 % indicating a short more humid period (maximum: 77 %; Fig. 4, Tab. S2). Starting at AD 1740, amounts of *Nothofagus* pollen finally increased to 47 % at AD 1995 while Poaceae pollen grains simultaneously decreased indicating stronger aridity.

Lacustrine signal

Biogenic Matter

The amount and chemical composition of biogenic matter and the diatom record are used to infer Holocene environmental conditions in the lake. TOC is a mixture of lacustrine algal biomass, aquatic macrophytes and terrigenous influx (Mayr et al., 2005). Therefore, lacustrine biomass is best archived by BSi documenting a steady increase from 8 % (base of unit B) to 61.2 % (subunit Ed; Fig. 4, Tab. S2). Assuming minimum effects of dissolution for biogenic opal, documented by good diatom preservation, we consider an increase of the trophic state throughout the Holocene. This process is interrupted by the sandy layers probably introducing additional nutrients into the lake and causing pronounced increases in BSi following both events (Fig. 4). Moreover, changes in diatom-species composition as well as in absolute diatom abundance during and after these events are evident (Fig. 5).

Decomposition during and after deposition mainly affected algal organic matter (TOC values). The TOC record starts with a mean of 2.3 % during unit B (Fig. 4, Tab. S2). An abrupt increase at the transition to unit C leads to maximum values of 9 % (mean: 5.5 %) during unit C and a subsequent decrease to 2.5 % at the onset of unit D. Since then, TOC increased steadily to 16.3 % at 3000 cal. BP (top of subunit Eb; Fig. 4) with evidence for dilution by tephra and sandy layers as in the BSi record. A marked drop in TOC to a mean of 12.5 % occurred at 2870 cal. BP, after which it started to increase again towards the top with a maximum of 18 % in subunit Ed at AD 1100 (Tab. S2). In a similar way to BSi, pulses of higher TOC follow the sandy layers, likely linked to eutrophication. This trend is less pronounced for S1 than for S2 (Fig. 4).

Information about the composition of organic matter and its terrestrial vs. lacustrine source is derived from TOC/TN in combination with δ^{13}C values (Fig. 4). Mean TOC/TN ratios vary between 4.2 and 11.1 (Tab. S2). In general, TOC/TN ratios <10 are interpreted as originating from lacustrine organic matter (Meyers, 2003). Higher values obtained during a monitoring study at Laguna Azul (Mayr et al., 2005) suggest either an admixture of reworked littoral sediments (TOC/TN: 8–11), submerged aquatic macrophytes (26–38), terrestrial plants (23–142) or organic matter from terrestrial soils (10–14). This can be resolved by using δ^{13}C values (Fig. 4), which indicate that modern aquatic macrophytes of Laguna Azul and littoral sediments are characterized by δ^{13}C values >-22.5 ‰, while values <-22.5 ‰ are typical for terrestrial plants, soils and profundal sediments of algal origin (Mayr et al., 2005). The δ^{13}C values of the sediment record are always <-23 ‰ (Fig. 4). They document a steady increase from the base of unit B (-29.3 ‰) to the top of subunit Eb (-26.0 ‰) with one distinct interruption during unit C, where δ^{13}C values decrease to a mean of -31.2 ‰. Only during this lithological unit TOC/TN ratios >9.4 occur (Tab. S1). A traditional interpretation (e.g., Meyers and Lallier-Verges, 1999) would conclude that such TOC/TN ratios indicate higher admixtures of vascular plants. However, recent studies have shown that algal organic matter in crater lakes with natural eutrophication can also exhibit TOC/TN ratios >10 due to N-limiting conditions (Heyng et al., 2012). Eutrophication and/or meromictic conditions can lead to δ^{13}C values below -30 ‰ due to microbial degradation of organic matter (Braig et al., 2013; Heyng et al., 2012; Hollander and Smith, 2001) explaining the observed values in unit C. The lack of correlation between TOC and BSi data during this unit further confirms that sedimentary organic matter is not only controlled by photosynthetic productivity but also by microbial sources and processes of decomposition.

The nitrogen isotope ratio (δ^{15}N) also reflects the source of organic matter, the isotopic signature of dissolved inorganic nitrogen (DIN) and lake internal processes such as denitrification. Values between 2 and 6 ‰ characterize modern terrestrial plants in the catchment area of Laguna Azul (Mayr et al., 2005). The δ^{15}N record (Fig. 4) marks a trend from low mean values (2.8 ‰) in unit B to more positive values in unit C (mean: 5.9 ‰). Then δ^{15}N mean values decrease to 5.1 ‰ (subunit Eb). At the transition to subunit Ec, a negative shift to a mean of 4.1 ‰ is recorded. Like the

TOC/TN ratio, this value remains almost constant towards the top (Fig. 4, Tab. S2). For the base of lithological unit B, low $\delta^{15}N$ values indicate little nitrate utilization and denitrification, which would cause a shift towards more positive values. TOC/TN ratios suggest predominance of lacustrine production. This indicates a lake at an early stage of evolution with low availability of nitrate or less intense denitrification compared to unit C. In this unit, TOC/TN ratios increase possibly due to loss of nitrogen related to enhanced microbial denitrification, which increases $\delta^{15}N$ values as evidenced by positive $\delta^{15}N$ excursions (Braig et al., 2013). This interpretation agrees with the strong decline of $\delta^{13}C$ and high concentration of TS (Fig. 4). Most likely, this is the result of methanogenesis and an expression of pronounced meromixis during unit C. Related anoxic conditions favour denitrification, increase the TOC/TN ratio and are indicated by high amounts of TS. The $\delta^{15}N$ values decrease from unit D to the Eb/Ec transition. Since 2800 cal. BP they remain almost constant documenting a decrease in nitrate utilization by phytoplankton and denitrification (Fig. 4).

Redox conditions

In the hypolimnion of lakes with seasonal or permanent anoxia (meromixis) reducing conditions are often observed under eutrophic conditions causing oxygen consumption and aerobic mineralization (Cohen, 2003). This modifies the primary sediment composition and produces distinctive secondary minerals with redox-sensitive elements such as Fe, Mn and S (Figs. 3, 4). After all the oxygen is depleted, slower anaerobic decomposition starts with processes like methanogenesis, denitrification and sulphate reduction. The latter causes the production of hydrogen sulphide (H_2S) which reacts with Fe to form pyrite (FeS). This mineral is well preserved and causes, together with high organic carbon content, the black sediment colour.

Considering black colour as a first indication for anoxia, lithological units B and C discriminate as such from the entire record (Fig. 2). Moreover, TS values and Fe/Ti ratios are elevated for both units and suggest the presence of pyrite (Figs. 3, 4, Tab. S2), which has been detected by XRD analyses for both units (Tab. S3). From unit D onwards, an oxic type of sediment composition prevails (Fig. 2). The lack of pyrite is confirmed by low TS values, low Fe/Ti ratios (Figs. 3, 4) and olive to brown sediment colours (Fig. 2). Distinct peaks in TS are recognized only in relation to sandy layer S2 (3200 cal. BP) and at 2800 cal. BP (Fig. 4).

The Fe/Mn ratio combines the two redox-sensitive elements Fe and Mn, where higher values indicate increased anoxia (Fig. 3). We distinguish five maxima of two different types: three maxima are >1000 years long and centred on 11,600, 10,000 and 1500 cal. BP while two ~300 year-long maxima are centred on 5500 and 3100 cal. BP (Fig. 3). Evident from Fe/Mn and black colour, unit C is the result of most pronounced anoxic conditions. This is supported by highest values for TS, high Fe/Ti ratios and most negative $\delta^{13}C$ values (Figs. 3, 4, Tab. S2). The latter are indicative for methanogenesis and suggest meromictic conditions. Furthermore, very high $\delta^{15}N$ values during unit C indicate denitrification (Fig. 4), which also explains the elevated TOC/TN ratio with a mean of 11.1 for unit C.

After unit C (mean Fe/Mn: 69.7) this redox-indicating ratio decreased towards subunit Eb with a mean of 26.3. At the same time, the Mn/Ti ratio increased in unit D (Fig. 3, Tab. S2). Such redox conditions are characteristic for oligotrophic lakes without pronounced anoxia. At 3000 cal. BP the situation changed again and Fe/Mn increased to >45 for subunits Ec and Ed, possibly related to re-establishment of anoxia in the hypolimnion due to increasing trophic conditions.

Diatoms

Almost all diatoms, 85 % of our record, are alkaliphilous or alkalibiontic species typical of neutral or basic lakes in a semiarid climate. This is in agreement with monitored pH values of 8.5–9.0 (Zolitschka et al., 2006). The diatom record subdivides into four diatom zones (DZ1–DZ4; Fig. 5). DZ1 is dominated by *Thalassiosira patagonica* (maximum: 85.1 % at 9020 cal. BP), a very small planktonic species that tolerates high conductivities (Wille et al., 2007). Additionally, the pioneer epiphytic species *Pseudostaurosira subsalina* is present with up to 15.3 %. Both species are indicative of saline conditions, which can be related to a negative water balance with a low lake level.

In DZ2 the diatom assemblage changes to dominance of epiphytic *Arcanodiscus platti* (48 %) and *Cocconeis euglypta (*17 %). Both species have wide ecological tolerances and point to freshwater conditions with higher lake levels supporting the growth of macrophytes in flooded areas. DZ3 is dominated by periphytic *Staurosira venter* (>90 %), which tolerates fluctuations of lake levels and salinities indicating a higher trophic status. The diatom assemblage from the exposed lake-level terrace dated to 1220 +70/-130 cal. BP (Fig. 1; Tab. 1) is entirely composed of *Staurosira venter* suggesting formation during DZ3. Uppermost DZ4 (since AD 1780) is dominated by planktonic *Stephanodiscus parvus* indicative of eutrophic conditions. The final step of eutrophication in the 20th century is marked by an exponential increase of absolute diatom abundance (Fig. 5). Changes in habitats from benthic to planktonic indicate a loss in littoral environments in response to a lake-level lowering. Simultaneously, a change of nutrient preferences from mesotrophic to eutrophic occurred. Lower lake levels caused eutrophication as well as calcite precipitation (TIC10) and likely were triggered by the post-LIA temperature increase of the "Current Warm Period" (CWP) documented as +2.5 °C (summer) and +1.4 °C (annual) temperatures for 1931–1990 at Rio Gallegos (Villalba et al., 2003). Since we observed a c. 11 m lake-level drop at close-by Laguna Potrok Aike since the 1890s (Haberzettl et al., 2005; Ohlendorf et al., 2013), the most conclusive regional cause for modern lake-level lowering is climatic.

Hydrological signal

Under the prevailing semiarid climate at Laguna Azul direct rainfall is of little influence on lacustrine hydrology. As the lake has no tributary, groundwater inflow, favoured by rapid infiltration through porous and fissured volcanic rocks, and evaporation, mainly controlled by SHW intensity, determine the lake's water budget. As no inflow exists, we regard clastic sediment transfer into the lake as a hydrological proxy related to wave erosion (WE) of Ti- and Ca-bearing alkali-basaltic rocks at the shoreline.

Periods of increased shoreline erosion are evident via elevated magnetic susceptibility as well as by high Ti and Ca contents at the end of lithological unit B (WE1: 10,400–10,100 cal. BP) and in early unit D (WE2: 8300–7500 cal. BP) (Figs. 3, 6). Shorter and event-like erosive periods follow with sandy layers S1 (WE3: 5500 cal. BP), S2 (WE4: 3200 cal. BP) and WE5 centred at 1300 cal. BP. We interpret this mobilization of littoral sediment as a consequence of rising and falling lake levels.

The signature of lithological unit A (pyroclastic material) is regarded as the external geochemical background signal (high Ti, Ca, DBD and MS) for wave erosion. During WE1, these parameters are relatively pristine as the lake is still at an early stage of lacustrine evolution. This changed since WE2, when increased TIC values document the presence of carbonates, e.g. linked to the formation of lacustrine tufa. Lacustrine tufa (beach rock) is observed on shoreline rocks of Laguna Azul formed by photosynthetic algae and cyanobacteria.

In addition to lakeshore erosion, carbonates also precipitate from the water column as calcite ($CaCO_3$). This process intensifies when the lake level lowers due to enhanced aridity causing higher concentration of soluble elements in the waterbody. As both, TIC and the Ca/Ti ratio, are influenced by calcite precipitation (Fig. 3), comparing them allows $CaCO_3$ to be distinguished from siliciclastic Ca that entered the sediment, e.g. as plagioclase (cf. Tab. S3). The latter has a constant Ca/Ti ratio (cf. WE1) unless other minerals are added. This effect is documented by the two Ti-depleted tephra layers causing peaks in Ca/Ti but no comparable peaks for Ti and TIC (Figs. 2, 3), suggesting that only siliciclastic Ca is added to the system. If Ca/Ti increases parallel to TIC, autochthonous calcite precipitates. However, if TIC is peaking without response of Ca/Ti, other carbonaceous minerals are responsible for the additional inorganic carbonate. This can be related to siderite ($FeCO_3$) under anoxic conditions, to rhodochrosite ($MnCO_3$) under less anoxic conditions and to potassium carbonate or potash (K_2CO_3) under extremely saline conditions (Cohen, 2003).

The record of Laguna Azul is characterized by ten distinct periods of elevated TIC (TIC1–TIC10 in Figs. 3, 6) of which seven link to calcite precipitation. TIC1 (11,600–10,800 cal. BP) is not associated with any change in Ca/Ti (Fig. 3), thus the presence of calcite is unlikely. Based on elevated Fe/Ti ratios, which point to an additional source of Fe, and in combination with a Fe/Mn peak indicating anoxic conditions, the formation of siderite is regarded as the cause for TIC1. XRD analyses confirm the presence of pyrite for TIC1 (Tab. S3) supporting the presence of anoxic conditions. However, no evidence of siderite or other carbonate minerals was detected, presumably because they occur only with minor contributions.

Also TIC2 (10,000–9600 cal. BP) does not coincide with siliciclastic input (Fig. 3). However, a peak of Ca/Ti suggests a link to calcite precipitation. Additionally, and according to the pronounced maximum of Fe/Ti, siderite has to be regarded as present (Fig. 3), which is supported by Fe/Mn and the presence of pyrite (Tab. S3). Moreover, Mn/Ti and K/Ti show peaks, which may be related to carbonate minerals like rhodochrosite and potash. Especially the latter needs highly saline conditions close to desiccation (Cohen, 2003), which would be supported by the salt-tolerant diatom *Thalasiosira patagonica* (Fig. 5). Due to their low concentrations, neither of these minerals could be verified mineralogically. TIC3 (8300–7600 cal. BP) occurs with a pulse of minerogenic matter as Ti and Ca increase together (Fig. 3). As Ca/Ti responds positively, we conclude that calcite is present. For the second half of TIC3, the presence of rhodochrosite is possible because Mn/Ti increased. TIC4 (5500 cal. BP) coincides with sandy layer S1 (WE3), pronounced Ca and Ti maxima but no response in Ca/Ti. Therefore, carbonates are lacking and eroded volcaniclastics are regarded as the source for TIC4 (Fig. 6). TIC5 (4700 cal. BP) has no corresponding responses for Ca, Ti or Fe. Elevated Mn/Ti ratios suggest rhodochrosite as carbonate mineral (Fig. 3). With TIC6 (3800 cal. BP) lacustrine conditions changed. Since c. 4000 cal. BP, calcite became the dominant carbonate mineral under increasingly eutrophic conditions (change from DZ2 to DZ3) with anoxic bottom waters as indicated by rising Fe/Mn (Fig. 3). Additionally, non-silicate Ca is documented in the system by a step-like increase of Ca/Ti. Still rhodochrosite seems to contribute to carbonates as indicated by a peak of Mn/Ti related to TIC6. TIC7 (3200 cal. BP) is linked to sandy layer S2 (WE4). A negative amplitude of Ca/Ti relates to siliciclastic deposition without carbonaceous Ca. Like for TIC4, the explanation is wave erosion. TIC8 (2200 cal. BP) is distinctly assigned to lacustrine calcite precipitation, as confirmed by XRD analyses at 2180 cal. BP (Tab. S3). Calcite is also the reason for TIC9 (1300–600 cal. BP) and TIC10 (last 50 years; Fig. 3).

Summarizing the hydrological signal of Laguna Azul, there are seven phases that relate calcite with lower lake levels while three (TIC1, TIC4, TIC7) are unrelated. The most prominent low lake-level event (TIC10) occurred during recent decades and is attributed to the CWP. The second and third major low lake levels date to 2200 (TIC8) and 1000 cal. BP (TIC9) corresponding by age to the “Roman Climatic Anomaly” (RCA) and the MCA documented for European records, respectively.

The lacustrine circulation type is another link to the hydrological setting. During units B and C as well as during subunits Ec and Ed, Fe/Mn suggests anoxic conditions. To achieve such conditions at least seasonally, the water column needs to be stratified. A surplus of organic matter provided by higher lacustrine productivity provokes oxygen consumption during decomposition, eventually leading to endogenic (biogenic) meromixis. Such processes are considered responsible for anoxia of the last 3000 years. However, these biogenic anoxia are less pronounced compared to those of unit B and especially unit C. During the early lake history permanent anoxia was established under fully meromictic conditions accompanied by methanogenesis despite low lacustrine productivity (oligotrophic–mesotrophic); a development explained by ectogenic meromixis (Hakala, 2004). Presumably triggered by a distinct increase of climate-induced evaporation, the lake level had fallen and salinity increased. Thus, density of the bottom water increased and stabilized the water column to form a permanent stratification. Without holomixis, strong anoxia established in the hypolimnion and caused ectogenic meromixis.

Evolution of a young crater lake

During the early stage of lake evolution, the inner slopes of the crater stabilized by mass wasting causing deposition of volcaniclastic sediments (unit A) in the central lake basin. The Early Holocene onset of lacustrine sedimentation (unit B) is transitional from clastic to organic sediments (Figs. 2, 6). According to the SHW intensity proxy (*Nothofagus*) and chironomid-based mean annual temperature (MAT) reconstructed at nearby Laguna Potrok Aike (Massaferro and Larocque-Tobler, 2013), the first half of unit B has low Lateglacial temperatures and SHW intensity was high. This is supported by an oligotrophic, shallow and meromictic lake (Fig. 6), where meromictic conditions are indicated by higher Fe/Mn and saline conditions (halophilous diatoms in DZ 1; Figs. 3, 5).

At 11,400 cal. BP TIC1 is linked to elevated Fe/Ti (Fig. 3) and indicates siderite. The end of TIC1 is defined by decreasing *Nothofagus* pollen amounts pointing to less intense SHW. Thus, less wind-induced evaporation caused the water level to rise, probably supported by increased precipitation. The lake freshened and anoxia disappeared. Deposition of minerogenic components indicates a rising lake level mobilizing pyroclastic lakeshore sediments via wave erosion (WE1; Fig. 6). High counts for Ti and Ca correspond geochemically to volcaniclastica of unit A.

With the onset of unit C, MAT reached its Early Holocene maximum coinciding with an increase in *Nothofagus* pollen amounts and maximum saline conditions documented by halophilous diatom *Thalassiosira patagonica* (Figs. 5, 6). A lake-level drop is documented by precipitation of calcite, siderite, rhodochrosite and potash (TIC2), the latter associated with highest salinity or desiccation (cf., Zhang et al., 2013). Simultaneously, stratification of the water column established after solutes increased in the hypolimnion (maximum of halophilous diatoms) initiating ectogenic meromixis (cf., Hakala, 2004), evidenced by presence of pyrite (Tab. S3) with high TS and Fe/Mn (Fig. 3). Furthermore, negative $\delta^{13}C$ values and a positive shift in $\delta^{15}N$

indicate methanogenesis and denitrification, respectively (Fig. 4). Altogether, this points to increased zonal winds accompanied by higher evaporation under increased MAT.

The transition to unit D is characterized by a salinity decrease indicated by diatoms in response to termination of meromixis indicated by lower Fe/Mn (Figs. 5, 6). Higher minerogenic contributions to the sediment (Ti, Ca) document lakeshore erosion (WE2; Fig. 6) and flooding of the littoral zone (Fig. 1). Simultaneously, TIC3 marks the onset of unit D resulting from high Middle Holocene temperatures and increased lacustrine productivity (Fig. 3). In the second half of unit D minerogenic matter and carbonates decline while lacustrine productivity continues to increase (Fig. 4). These changes are interpreted as response to decreasing SHW intensity.

A general change from blackish to brownish sediment characterizes the onset of unit E (Fig. 2). Subunits Ea and Eb continue with low *Nothofagus* pollen amounts and high MAT (Fig. 6). TIC4 occurred simultaneous with WE3. Thus, the majority of Ca is bound to minerogenic matter (Ca/Ti; Fig. 3). The onset of subunit Eb is characterized by a distinct increase in lacustrine productivity (Fig. 4, Tab. S2). Diatoms indicate an increasing trophic state from subunit Eb towards the top. TIC5 is not linked to calcite but probably to rhodochrosite (Mn/Ti; Fig. 3). We interpret this as related to low SHW intensity with positive water balance for subunits Ea and Eb.

At 3800 cal. BP during ending subunit Eb, a drop in MAT to its Late Holocene mean occurred (Fig. 6). This transition is evident in the diatom record with a prominent shift from planktonic and epiphytic (DZ2) to benthic (DZ3) lifeforms (Fig. 5), and in Ca/Ti with a lower mean of 1.9 % before and 3.0 % after 3800 cal. BP (Fig. 3). The now prevailing benthic diatom *Staurosira venter* tolerates frequent lake-level fluctuations and is adapted to higher trophic states (Fig. 5). We interpret this step like increase of Ca/Ti as a consequence of higher lacustrine productivity explaining the first calcite-dominated TIC6 probably with admixture of rhodochrosite (Fig. 3). TIC7 coincides with sandy layer S2 (WE4); extra Ti and Ca of basaltic origin links to higher lake levels and wave erosion (Fig. 6).

Following the temperature drop at 3800 cal. BP, *Nothofagus* pollen amounts started to increase heralding the SHW intensity change at 3000 cal. BP, which marks the transition to subunit Ec (Tab. S2; Fig. 6). Interpreted as the result of SHW intensity increase, windier conditions with more evaporation and less precipitation caused the lake level to drop culminating in calcite-dominated TIC8 (Figs. 3, 6). A falling lake level further supported higher productivity as indicated by diatoms of DZ3 causing seasonal anoxia due to intensified decomposition of organic matter at the lake floor mirrored by a positive shift in Fe/Mn (Figs. 3, 6). For TIC8 (RCA) and the following warm/dry events related to TIC 9 (MCA) and TIC10 (CWP) we use names established for contemporaneous climatic events of the Northern Hemisphere.

The transition to subunit Ed is marked by WE5 caused by a higher lake level at 1300 cal. BP coinciding with the subaerial lake-level terrace composed of *Staurosira venter* and dated to 1190 ±100 cal. BP (Fig. 1, Tab. 1). This period corresponds to the “Dark Age Cold Period” (DACP) of the Northern Hemisphere (Helama et al., 2017). Immediately after WE5, TIC9 occurred with eutrophic conditions as documented by appearance of *Staurosirella pinnata* (Fig. 5). This is related to a more negative water balance with concentration of nutrients and calcite precipitation during the MCA (TIC9)

Centuries later, maximum Poaceae and a decrease of *Nothofagus* pollen amounts indicate moister and less windy conditions linked to distinctly lower Fe/Mn from AD 1550–1850 (Fig. 4), a period related to the LIA. During the second half of the 20th century highest carbonate values occur (TIC10=CWP) coinciding with a decrease of lake levels (Fig. 3). The final part of the record is characterized by onset of human activities since AD 1830 corroborating Mayr et al. (2005).

Mechanisms of climate change

Despite the Southern Hemispheric summer minimum of solar insolation at 10,000 cal. BP (Berger and Loutre, 1991), the Early Holocene was the warmest period in southern South America. At Laguna Azul this is evidenced by strongest zonal winds with maxima at 11,600 and 9000 cal. BP. Early Holocene weakening of the thermohaline circulation in the Northern Hemisphere reduced heat transfer from the South Atlantic to the North Atlantic. Thus, thermal energy increased in Southern Oceans causing an air-temperature rise in the Southern Hemisphere (Ganopolski et al., 1998; Hodell et al., 2001).

A similar mechanism explains the start of the Neoglacial in South America. Although the Southern Hemisphere experienced increased insolation, the Neoglacial cooling is observed since at least 5000 cal. BP (Glasser et al., 2004). The reason is cooling of the Northern Hemisphere since 9000 cal. BP (Berger and Loutre, 1991). In turn, increased thermohaline circulation resulted in heat export from the South Atlantic to the North Atlantic triggering sea-ice growth around Antarctica and glacial advances on the continents. This caused global feedbacks at the end of the Middle Holocene, such as the termination of the African Humid Period (Ganopolski et al., 1998) or the establishment of modern El Niño-Southern Oscillation (ENSO) frequencies (Clement et al., 1999; Moy et al., 2002; Sandweiss et al., 1996).

In contrast to the Lateglacial-Holocene transition, temperature and zonal wind intensity are decoupled since 7000 cal. BP with strengthened and poleward shifted

SHW (Varma et al., 2012). This agrees with more pronounced ENSO frequencies in response to increased insolation (Clement et al., 2000) and reached highest intensity during the last 3500 years (Moy et al., 2002; Villa-Martínez et al., 2003).

In synthesis, Fletcher and Moreno (2012) suggest zonal changes of SHW on millennial timescales between 14,000 and 5000 cal. BP that switched to a centennial pattern after 5000 cal. BP, controlled by intensified ENSO (Moreno et al., 2014). Markgraf (1998) developed a comparable conclusion, linking modern seasonal shifts of SHW to a pattern that established 4000 cal. BP when seasonality of insolation increased in the Southern Hemisphere. These forcing mechanisms operate at different strengths and timescales (Bentley et al., 2009) and their causal relationships are not yet completely understood (Garreaud et al., 2013). Additional centennial-scale variability is observed in our record and well represented by geochemistry (TIC maxima) characterizing lake level low stands, i.e. warm/dry and more windy conditions with higher evaporative stress such as the RCA (TIC8), the MCA (TIC9) and the CWP (TIC10).

Regional Variability of Southern Hemispheric Westerlies

The search for a better knowledge about SHW variability stimulated research in Patagonia, the only continental landmass that intersects with the SHW wind belt. To learn how climatic changes observed at Laguna Azul contribute to the understanding of SHW variability, we compare our findings with other records from South America (Fig. 7). Overall, studies agree that the core region of SHW migrated latitudinally between equatorward positions during glacial and poleward positions during interglacial conditions (Toggweiler et al., 2006). Currently, SHW vary seasonally between 40–60 °S (Kohfeld et al., 2013), while an expanded band (30–60 °S) is assumed for the Holocene (Fletcher and Moreno, 2011).

At Laguna Azul we observed four intervals with varying SHW modes during the Holocene. Low lake levels due to increased SHW intensity with high evaporation rates occurred from 10,100–8300 cal. BP with lowest lake levels and development of ectogenic meromixis and since 3000 cal. BP creating seasonal anoxia in combination with eutrophication. Low zonal winds with increased precipitation caused higher lake levels from 11,200–10,100 and from 8300–3000 cal. BP (Figs. 6, 7)

A less arid period with weaker SHW marks the Early Holocene (11,200–10,100 cal. BP) at Laguna Azul. Simultaneously, wetter conditions were reported from the lee-sites Rio Rubens (52 °S: -0.5) (Markgraf and Huber, 2010), Laguna Potrok Aike (52 °S: -0.6) (Hahn et al., 2013) and Lago Cardiel (49 °S: -0.8) (Quade and Kaplan, 2017). The second value provided in brackets is the correlation coefficient between precipitation and zonal wind speed according to Moreno et al. (2014). Whether the SHW moved poleward or equatorward during the Early Holocene can be checked. Further to the north, Lago El Salto (42 °S: +0.8) turned drier in a luv position indicative of a southward shift of SHW (Moreno and Videla, 2016). There is additional evidence from Lake Tamar (53 °S: +0.8) of wet conditions from a luv position (Lamy et al., 2010), while Isla de los Estados in a lee position (55 °S: -0.8) was dry (Björck et al., 2012), both indicative of stronger SHW. For the marine record Palmer Deep (65 °S, luv of Antarctic Peninsula) no signs of SHW presence were recognized (Domack et al., 2001). We conclude that the core of SHW was located between 53–60 °S in the Early Holocene in agreement with the SHW position (57 °S) suggested by Quade and Kaplan (2017) (Fig. 7).

For the early Middle Holocene Laguna Azul recorded lowest lake levels and ectogenic meromixis as consequence of highest zonal winds (10,100–8300 cal. BP).

A lake level drop of 30 m is also documented for Laguna Potrok Aike (52 °S: -0.6) from 9300–6900 cal. BP (Anselmetti et al., 2009; Gebhardt et al., 2012; Kliem et al., 2013; Zolitschka et al., 2013) coincident with most intense SHW reconstructed from long-distance transport of AFT pollen peaking at 8600 and 7500 cal. BP (Fig. 7). Further north, Lago El Salto (42 °S: +0.8) and Lago Condorito (41 °S: +0.6) were drier from 11,600-7600 and 10,000-7600 cal. BP, respectively (Moreno et al., 2010; Moreno and Videla, 2016) indicating weaker SHW. At 46 °S Lago Castor experienced a minor increase in SHW intensity (Van Daele et al., 2016), while Lago Cardiel (49 °S: -0.8) is characterized by decreasing lake levels from 10,000–7800 cal. BP (Quade and Kaplan, 2017). South of Laguna Azul, Isla de los Estados (55 °S: -0.8) experienced no SHW influence until 7200 cal. BP (Björck et al., 2012) (Fig. 7). In summary, between 10,000 and 7500 cal. BP the core region of SHW migrated northward to 50–52 °S, in agreement with the SHW position of 51 °S reconstructed for Lago Cardiel (Fig. 7). More northern sites document little (Lago Castor) or no (Lagos El Salto and Condorito) influence of a SHW intensity increase.

For the late Middle Holocene, a distinct poleward shift of SHW to 65 °S is documented until 3360 cal. BP for Palmer Deep (Domack et al., 2001). Furthermore, an increase in SHW intensity was noted for Isla de los Estados (55 °S: -0.8) reaching wind-intensity maxima between 4600–3300 cal. BP (Björck et al., 2012) (Fig. 7). To the north, Lago Condorito (41 °S: +0.6) was wetter after 7000 cal. BP (Moreno et al., 2010), while Lago Cardiel (49 °S: -0.8) recorded a higher lake level between 7500–5000 cal. BP (weaker SHW) and a lake level lowering (stronger SHW) from 5000–3300 cal. BP (Quade and Kaplan, 2017). Lago Castor (46 °S) experienced strengthened SHW (7500–3800 cal. BP; Fig. 7) with a maximum from 5000–3800 cal. BP (Van Daele et al., 2016). On the other hand, Laguna Potrok Aike (52 °S: -0.6) documents a lake level rise and lower *Nothofagus* pollen amounts (6900–3300 cal. BP) coincident with decreasing SHW intensity (Mayr et al., 2007b), just like the record from Laguna Azul (this study) between 7500–3000 cal. BP. In summary, strong SHW intensities were recorded from 65–41 °S. This is at the same time when Lagunas Azul and Potrok Aike experienced less windy conditions than before. One possible explanation is an expansion of the SHW belt with highest zonal winds at northern and southern margins while the central part at 52 °S weakened.

Not only had the southern location of SHW reached the Drake Passage during the late Middle Holocene, also gradually colder conditions established in Patagonia since the onset of the Neoglacial between 7000–5000 cal. BP. There is evidence from glaciers of the South Patagonian Icefield (50 °S) expanding since 5800 cal. BP (Porter, 2000), moraines at Lago Argentino (51 °S) document glacial advances after 6000 cal. BP (Kaplan et al., 2016) and a sediment record obtained from Almirantazgo Fiord (54 °S) shows first glacial re-advances at 5700 cal. BP (Bertrand et al., 2017). Furthermore and related to increased precipitation, a stalagmite developed in the luv of the superhumid Andes in Marcelo Arevalo Cave (53 °S) after 5700 cal. BP (Schimpf et al., 2011). Although the onset of the Neoglacial evidences colder temperatures and thus suggests a northward migration of SHW since 7000 cal. BP, the record of Palmer Deep at 65 °S still documents high SHW intensity until 3360 cal. BP (Domack et al., 2001) – a contradiction that needs to be resolved.

During the Late Holocene, marine productivity decreased at Palmer Deep (65 °S) after 3360 cal. BP. At Isla de los Estados (55 °S: -0.8) weaker SHW occurred after 3300 cal. BP (Björck et al., 2012) as well as at Lake Tamar (53 °S: +0.8) after 5500 cal. BP (Lamy et al., 2010) and at Lago Fagnano (54 °S: -0.6) after 6000 cal. BP (Waldmann et al., 2010). The response at Punta Yartou (54 °S: +0.6) shows wetter and colder conditions after 5060 cal. BP (Mansilla et al., 2016) and at Laguna Azul (52 °S: -0.8) more *Nothofagus* pollen, both indicative of higher SHW intensity. Lago

Castor (46 °S: transitional) shows a decrease in sortable silt (Van Daele et al., 2016) and Lago Cardiel (49 °S: -0.8) higher lake levels, i.e. less zonal winds for both sites since 3300 cal. BP. In the north, Lagos El Salto (42 °S: +0.8) and Condorito (41 °S: +0.6) continued to have wetter conditions (Moreno et al., 2010; Moreno and Videla, 2016) as does marine site GeoB3313-1 (41 °S: +0.8) after 4000 cal. BP (Lamy et al., 1999; Lamy et al., 2010). In conclusion, weaker SHW south of 54 °S is associated with increased SHW intensity at Laguna Azul, decreased SHW intensity at Lagos Cardiel and Castor (Fig. 7) and continuously high zonal winds to 41 °S. Whether this is in response to the SHW belt with its windier margins being shifted northward following the onset of Neoglaciation with a delay or the result of other processes remains an open question.

Overprinting the millennial SHW pattern, there are century-long cold/wet and warm/dry periods during the Late Holocene. Their onset coincides with a distinct MAT decline (3800–3200 cal. BP; Figs. 6, 7). Almost simultaneously, the proxy for wind intensity (*Nothofagus*) indicates the onset of higher zonal winds for Lagunas Azul and Potrok Aike, while independent SHW proxies decrease for Islas de los Estados and Lago Castor (Fig. 7). Although MAT displays no major variability for the Late Holocene, sediments evidence three distinct periods with lower lake levels centred at 2200 and 1000 cal. BP and during the last century (Fig. 6) coeval to Northern Hemispheric RCA, MCA and CWP. Furthermore, we recognize the DACP and the LIA as pronounced moist periods with high lake levels and maximum expansion of Poaceae (Figs. 4, 6).

Best represented is the cool/wet LIA detected at many sites from Palmer Deep near Antarctica (Domack et al., 2001), via Lago Fagnano on Tierra del Fuego (Waldmann et al., 2010) towards the marine record GeoB-3313 off Chile (Lamy et al., 2010) with many Patagonian sites in between: Lagunas Potrok Aike (Haberzettl et al., 2005), Azul (this study), Las Vizcachas (Fey et al., 2009), Cháltel (Ohlendorf et al., 2014), Cari-Laufquén (Cartwright et al., 2011) and Lagos Guanaco (Moreno et al., 2010), del Desierto (Kastner et al., 2010), Cardiel (Ariztegui et al., 2010), El Salto (Moreno and Videla, 2016) and Puyehue (Boës and Fagel, 2008).

A number of records available for the last millennium also confirms a three partition in MCA, LIA and CWP: Lagos Puyehue (Boës and Fagel, 2008), El Salto (Moreno and Videla, 2016), del Desierto (Kastner et al., 2010), Guanaco (Moreno et al., 2009), Cipreses (Moreno et al., 2014), and Lagunas Potrok Aike (Haberzettl et al., 2005), Azul (this study) and Las Vizcachas (Fey et al., 2009). This picture is supported by regional paleohydric balance integrations from southeastern Patagonia documenting a positive water balance for the LIA (500–100 cal. BP) and a negative water balances for the CWP (since AD 1919) and the MCA (1400–500 cal. BP) (Echeverria et al., 2017). Moreover, temperature reconstructions on a continental-scale for South America reveal colder conditions from AD 1380–1920 (equivalent to the LIA), whereas two warmer phases were recognized for AD 1150–1320 (equivalent to the MWP) and for the CWP (Ahmed et al., 2013). Additionally, the pronounced warm/dry period of the RCA at Laguna Azul was recognized at other Patagonian lakes, such as Lagos El Salto, Cipreses and Guanaco (Moreno et al., 2009; Moreno et al., 2014; Moreno and Videla, 2016) pointing to overarching regional climatic control disregarding their luv/lee location west or east of the Andes.

The loss in zonal symmetry of SHW was suggested to be responsible for the onset of centennial climate fluctuations related to ENSO variability with teleconnections across South America (Fletcher and Moreno, 2012). This increase in ENSO frequency accelerated during the last 3800 years and peaks during the MCA (Moy et al., 2002). For the same time interval stronger linkages between SHW, insolation (solar activity, astronomical forcing) and ENSO were postulated by Kilian and Lamy (2012). Changes in solar activity seem to be capable of climate implications unrelated to zonal symmetry and follow a global character. A well-known example was the Maunder solar minimum, which together with large volcanic eruptions was one of the triggers responsible for the LIA (Owens et al., 2017).

Conclusions

Position and strength of SHW are documented by the multiproxy study of Holocene sediments from Laguna Azul in semiarid southeastern Patagonia highlighting millennial- to centennial-scale hydroclimatic variability. The lacustrine history of Laguna Azul started with higher lake levels in the Early Holocene (11,200–10,100 cal. BP), which are linked to weaker SHW reflected by generally increased moisture availability east of the Andes (cf., Mancini et al., 2008). During the Early Holocene, the core of SHW was located between 53–60 °S. From 10,100–8300 cal. BP low lake levels and high salinity document driest conditions. Together with anoxia and methanogenesis, evidence for ectogenic meromixis relate to highest SHW intensities centred around 50 °S with increased evaporation indicated by drier conditions east of the Andes (cf., Mancini et al., 2008). Between 8300–3000 cal. BP, an again higher lake level was linked to warmer and moister conditions at Laguna Azul indicative of less intense SHW. However, regional comparison documents an expansion of stronger SHW to 65–41 °S, a discrepancy that needs to be investigated by further studies. After 4000 cal. BP, MAT indicates the Neoglacial temperature drop. Lacustrine conditions became more variable with century-long warm/dry (RCA, MCA, CWP) and cold/moist (DACP, LIA) periods under generally increased SHW intensity. These short climatic anomalies are also known from sites west of the Andes and from the Northern Hemisphere. At 3300 cal. BP SHW pulled back from latitudes south of 54 °S and contracted to 54–41 °S.

Despite many environmental and climate investigations from southeastern Patagonia, substantial knowledge gaps still exist. To improve our understanding of SHW variability, an extended network of high-resolution terrestrial and marine records with quantitative reconstructions as well as reliable time control are mandatory to develop consistent interpretations. This includes the studied site, where high-resolution diatom and chironomid records would contribute additional quantitative reconstructions. Moreover, integration of critical sites by climate modelling would be beneficial to determine the different modes of forcing that control the climate of South America on a regional scale with influences on the entire Southern Hemisphere and beyond.

Acknowledgements

The authors thank the late Cristóbal Kennard, Capt. Jorge D. Moreteau and INTA Santa Cruz for assistance in organizing the logistics of fieldwork. The team at the ODP/IODP Bremen Core Repository is acknowledged for providing technical equipment and expertise as well as Thomas Frederichs and Christian Hilgenfeldt for access to their magnetic measuring bench. We thank Rolf Kilian for comments regarding Patagonian tephrochronology and Hans-Joachim Gregor for taxonomic identification of *Ruppia* seeds. Thanks also go to Julieta Massaferro and Maarten Van Daele for making available data from Laguna Potrok Aike and Lago Castor, respectively. Finally, we would like to thank Vera Markgraf for improving an earlier version of this manuscript, Vivienne Jones for her editorial support as well as two anonymous reviewers for their mindful and constructive comments and suggestions.

Funding

This is a contribution to the project “South Argentinean Lake Sediment Archives and modelling” (SALSA) funded within the framework of the German Climate Research Program (DEKLIM grants 01 LD 0034 and 0035) of the German Federal Ministry of Education and Research (BMBF). Additional financial support was provided by the German Science Foundation (DFG) in the framework of the Priority Program ‘ICDP’ (grants ZO 102/5-1, 2, 3).

Data

Multiproxy data from Laguna Azul as well as additional data are accessible via the PANGAEA data archiving and publication system at https://doi.pangaea.de/10.1594/PANGAEA.889673.

Contribution of authors

AL, BZ, CM, CO, FS, MF and TH participated in the fieldwork. HC provided volcanological background data and supported fieldwork logistically and politically. MF performed all geochemical and physical sediment analyses and picked samples for radiocarbon dating. SW carried out tephra analyses, AL and CM analysed stable isotopes, SJ and FS performed pollen analyses, NIM investigated diatoms and CO developed the age/depth model. BZ drafted the figures as well as the manuscript. All authors contributed to improve the manuscript. BZ, AL and FS are responsible for the study design.

Figures

Fig. 1: Study area in southern South America with locations mentioned in the text. Laguna Azul is site 18 and indicated by a black square (left). The expanded view of Laguna Azul (right) includes bathymetry with exposed lake-level terraces, coring sites, sampling locations and surrounding topography.

Fig. 2: Lithology of the composite record from Laguna Azul with lithological units (A to E) and subunits (Ea to Ed) vs depth displaying dry bulk density (DBD), magnetic susceptibility (MS), titanium (Ti), total organic carbon (TOC) and the age-depth model with radiocarbon dates (error bars are smaller than the triangle symbols) and modelled age (thick line) with 2σ error margins (thin lines). Also indicated are tephra layers AZU-T1 and AZU-T2 (T1,2) and sandy layers S1 and S2.

Fig. 3: Minerogenic sediment parameters vs time displaying titanium (Ti), total inorganic carbon (TIC) as a 7-point running mean (7PRM), calcium (Ca), and selected elemental ratios. Lithological units and subunits (A–Ed) are labelled and indicated by dashed horizontal lines. Also indicated are tephra layers AZU-T1 (T1) and AZU-T2 (T2) and the sandy layers (S1, S2). TIC maxima are numbered as TIC1–TIC10 and five periods with wave erosion (WE1–WE5) are labelled.

Fig. 4: Organic sediment parameters vs time displaying total organic carbon (TOC), biogenic silica (BSi), total organic carbon to total nitrogen molar ratio (TOC/TN_{molar}), total sulphur (TS), stable isotope records of nitrogen and carbon ($\delta^{15}N$, $\delta^{13}C$), and the pollen records of *Poaceae* and *Nothofagus*. Lithological units and subunits (A–Ed) are labelled and indicated by dashed horizontal lines. Also indicated are tephra layers AZU-T1 and AZU-T2 (T1, T2), sandy layers (S1, S2) and periods of meromixis (shaded in green).

Fig. 5: Percentage diagram of relevant diatom taxa vs time (Arc. platti = Arcanodiscus platti, *Cocc. eug. = Cocconeis euglypta, Cycl. men. = Cyclotella meneghiniana, Pseudo. subs. = Pseudostaurosira subsalina, Stephanod. parvus = Stephanodiscus parvus, Staur. pin. = Staurosirella pinnata, Thal. pata. = Thalassiosira patagonica*). Diatom zones (DZ1–DZ4) are labelled and marked by shaded horizontal bars and lithological units and subunits (A–Ed) by dashed horizontal lines. Also indicated are sandy layers (S1, S2). Trophic preferences (m: mesotrophic, e: eutrophic), diatom lifeforms and absolute diatom abundances are provided as well.

Fig. 6: Synthetic diagram of climatic and environmental proxies from Laguna Azul displaying selected parameters with environmental and climatic implications. Titanium (Ti) indicates minerogenic sediment flux from the crater slopes. Lacustrine biomass is represented by total organic carbon (TOC). Total inorganic carbon (TIC) is indicative of evaporation and representative for the lake level. $\delta^{13}C$ indicates methanogenesis and is related to an anoxic hypolimnion. The diatom *Thalassiosira patagonica* (*Thal. pata.*) is a proxy for salinity. Fe/Mn corresponds to redox conditions and *Nothofagus* pollen amounts to SHW intensity. For comparison, the chironomid-based mean annual temperature (MAT) from Laguna Potrok Aike is shown on its own independent time scale (Massaferro and Larocque-Tobler, 2013). Arrowheads point towards higher values. Lithological units and subunits (B–Ed) are labelled and indicated by dashed horizontal lines. Also indicated are tephra layers AZU-T1 and AZU-T2 (T1, 2) and sandy layers (S1, S2). Furthermore, five periods with wave erosion (WE1–WE5) and ten with maxima in total inorganic carbon (TIC1–TIC10) are labelled. The warm/dry periods of the “Roman Climate Anomaly” (RCA), the “Medieval Climate Anomaly” (MCA) and the “Current Warm Period” (CWP) are

labelled and marked by a horizontal bar shaded in red. The cold/moist “Dark Age Cold Period” (DACP) and the “Little Ice Age” (LIA) are labelled and marked by a horizontal bar shaded in blue. In addition, the initial lake phase and two meromictic periods are shaded in pink and green, respectively.

Fig. 7: Holocene millennial-scale SHW reconstructions for sites east of the Andes from south (left) to north. (A) Total annual flux (TAF) of silt grains at Isla de los Estados (Björck et al., 2012); (B) Long-distance and wind-delivered pollen amounts of *Nothofagus* for Laguna Azul (this study) and (C) for Laguna Potrok Aike (Wille et al., 2007); (D) Chironomid-based mean annual temperature (MAT) from Laguna Potrok Aike (Massaferro and Larocque-Tobler, 2013); (E) Hypothesized latitudinal migration of SHW for Lago Cardiel based on lake level variations (Quade and Kaplan, 2017); (F) Mean sortable silt (MSS) from Lago Castor (Van Daele et al., 2016). All data are smoothed with a 5-point running average (except E) and shown on their own independent time scales.

Table

Table 1: AMS radiocarbon dates from Laguna Azul calibrated with Clam 2.2 (Blaauw, 2010) and the southern hemisphere calibration curve SHCal13 (Hogg et al., 2013). Modelled ages (n.d.: not determined) were obtained with the smoothed spline option of Clam 2.2. Samples above the upper dashed line are not from sediment cores. Samples below the lower dashed line are artificially aged by volcanogenic CO_2.

Supplementary material

Tephra analysis and interpretation

Methods

The chemical composition of single glass shards was determined on polished thin sections by electron-probe microanalyses to obtain major element data. Prior to the preparation of thin sections, samples were cleaned with 30 % H_2O_2 to remove organic matter and then dried with ethanol. Measurements were carried out using a CAMECA SX100 (WDS) instrument at the GFZ German Research Centre for Geosciences (Potsdam, Germany). Operating conditions were 15 kV accelerating voltage, 20 nA beam current, a defocused beam of 15 µm diameter and peak counting times of 20 s except for Na (10 s). For instrumental calibration, the Lipari obsidian was used as reference material (Hunt and Hill, 1996; Kuehn et al., 2011). Individual analyses of glass shards with total oxide sums <95 wt. % were excluded. Data of accepted analyses for individual tephra layers were recalculated to 100 wt. % and are given as mean values with 1σ standard deviation of *n* glass shards (Tab. S1). Petrological classification is based on the total-alkali-silica (TAS) diagram (Le Bas et al., 1986).

Results

The sediment record from Laguna Azul contains two macroscopic volcanic ashes (Fig. S2). The lower tephra (AZU-T1 at 585.2 cm) is a white, fine-grained ash of 4–9 mm thickness with a maximum grain size of 150 µm. AZU-T1 mainly consists of colourless vitric glass shards of rhyolitic composition characterized by high silica (75.8 wt.%) and high potassium contents (4.0 wt.%; Tab. S1, Fig. S4). The mineral assemblage comprises plagioclase, orthopyroxene, amphibole, biotite and Fe-Ti-oxide phenocrysts. The upper tephra layer (AZU-T2 at 581.9 cm) is also a vitric white ash of 7–9 mm thickness with a maximum grain size of 100 µm. The composition of glass shards is rhyolitic with a silica concentration similar to AZU-T1 (76.1 wt. %) but with a distinctly lower potassium content (1.8 wt. %) (Tab. S1). Its mineral assemblage comprises plagioclase, orthopyroxene, rare amphibole and Fe-Ti-oxide phenocrysts. The third light layer at 580 cm turned out to be a mixture of fine-grained lake sediments with reworked tephra from AZU-T1 and AZU-T2 (Fig. S2). Radiocarbon dating of organic sediment between AZU-T1 and AZU-T2 at 583 cm yielded a ^{14}C age of 5280 ±50 BP and a modelled age of 6090 cal. BP (Fig. S2, Tab. 1).

Interpretation

The two tephra layers originate from different volcanic sources. Based on geochemistry of their glass shards (Fig. S4, Tab. S1), AZU-T1 (modelled age: 6160 cal. BP) is attributed to an explosive eruption of the Northern Austral Volcanic Zone (NAVZ) located ~400 km NW of Laguna Azul. AZU-T2 (modelled age: 6050 cal. BP) is related to an eruption of Mt. Burney located ~260 km W of Laguna Azul.

A literature survey revealed that such a succession of tephra layers has not been reported. There are, however, individual volcanic ash deposits from other locations that chronologically compare with AZU-T1 or AZU-T2. AZU-T1 might be related to a 60 mm thick tephra documented at Vega Ñandú (for location of sites: Fig. 1) radiocarbon-dated to 5700 -50/+140 cal. BP (Villa-Martínez and Moreno, 2007). The most likely candidate for correlation with AZU-T2 from Mt. Burney is a 1 mm thick tephra detected in the sediments of Lake Chandler dated to 5690 cal. BP (Kilian et al., 2003). Additional evidence for this tephra derives from an aeolian sequence near Lake Arturo. Here a 40 mm thick volcanic ash was deposited between two paleosols with bracketing ages of 6540 and 5550 cal. BP (Coronato et al., 2011). From Lake Ballena, a 35 mm thick Mt. Burney tephra was dated to 5440 -120/+140 cal. BP (Fontana and Bennett, 2012).

Analysis of biogenic silica

Biogenic silica (BSi) was analysed with the conventional automated leaching method (Müller and Schneider, 1993) and by applying a less time-consuming pressure pulping method with alkaline digestion in autoclaves. For both methods, BSi was subsequently detected by a continuous flow system with UV-VIS spectroscopy. The pressure pulping method yields better reproducibility with significantly lower standard deviations and has a higher throughput. This method, however, is applicable only to organic-rich sediments that are poor in minerogenic components, because siliciclastic components cause an overestimation of BSi values due to partial dissolution of silicates. Thus, for the lowermost part of the record (below 560 cm), where higher magnetic susceptibility points to clastic components, the conventional method was applied. For the pressure pulping method 3–5 mg of homogenized sample material were weighted into Teflon®-autoclaves. After addition of 20 ml 1 M NaOH, digestion was performed at 100 °C in a pressure pulping system for 2 or 4 h. The resulting solution was filtered, and an aliquot of 5 ml was diluted with 20 ml 1 M NaOH to determine BSi by UV-VIS spectroscopy. The residence time necessary for the pulping system was obtained by comparison with measurements of selected samples with the conventional method. In consequence, samples from the uppermost 200 cm were digested for 4 h, while a residence time of 2 h was applied for samples from 200–560 cm sediment depth. The amount of biogenic matter (BioM) is estimated as the sum of BSi and TOC, for the latter using the conversion factor of 2.13 (Dean, 1974).

Supplementary figures

Fig. S1: Composite record of magnetic susceptibility (MS) data as shown in Fig. 2 (left). Furthermore, MS of gravity core AZU 03/5 (green) and of piston cores AZU 03/4 (red and grey) and AZU 03/6 (blue) are plotted vs depth. Correlations are marked by lines.

Fig. S2: Photography of the core face between 587.5 and 578.5 cm sediment depth (lithological subunit Ea) with tephra layers AZU-T1 from the Northern Andean Volcanic Zone (NAVZ) and AZU-T2 from Mt. Burney with modelled ages. Additionally, the position of the radiocarbon age from 583 cm composite depth (Tab. 1) is indicated with radiocarbon as well as modelled ages.

Fig. S3: Results of unconstrained cluster analysis performed with eight representative organic and minerogenic sediment parameters: dry bulk density (DBD), magnetic susceptibility (MS), carbon to nitrogen ratio (TOC/TN), total organic carbon (TOC), total inorganic carbon (TIC) as a 7-point running mean (TIC_{7PRM}), total sulphur (TS), iron to manganese ratio (Fe/Mn_{7PRM}) and calcium to titanium ratio (Ca/Ti_{7PRM}). Lithological units and subunits are labelled as A–Ed and indicated by horizontal lines.

Fig. S4: SiO_2 vs K_2O diagram assigns the two distal tephra layers from Laguna Azul (AZU-T1, AZU-T2) to their respective sources by comparison with other archives in southern Chile and Argentina (Bitschene and Fernandez, 1995; Haberzettl et al., 2007; Haberzettl et al., 2008; Kilian et al., 2003; Naranjo and Stern, 1998; Stern, 1990).

Supplementary tables

Tab. S1: Microanalytical electron-probe data (wt. %) of individual glass shards from two distal tephra layers documented in the Laguna Azul sediment record and of the Lipari obsidian standard.

Tab. S2: Lithological units and subunits for the sediment record of Laguna Azul with corresponding depths and age ranges as well as arithmetic mean values for physical data (MS: magnetic susceptibility, WC: water content, DBD: dry bulk density), geochemical data (TC: total carbon, TN: total nitrogen, TS: total sulphur, TOC: total organic carbon, TOC/TN: organic carbon/nitrogen molar ratio, TIC: total inorganic carbon, BSi: biogenic silica), selected stable isotope ($\delta^{13}C$, $\delta^{15}N$), elements (Ti, Ca) and elemental ratios (K/Ti, Ca/Ti, Fe/Ti, Mn/Ti, Fe/Mn) as well as selected pollen (*Poaceae*, *Nothofagus*), absolute diatom abundance, sedimentation rate (SR), biogenic matter (BioM) and minerogenic matter (MM) (n.d. = not determined).

Tab. S3: Mineralogical composition of selected samples from different lithological units of Laguna Azul based on XRD analysis.

References

Ahmed M, Anchukaitis KJ, Asrat A, et al. (2013) Continental-scale temperature variability during the past two millennia. *Nature Geoscience* 6: 339-346.

Anselmetti FS, Ariztegui D, De Batist M, et al. (2009) Environmental history of southern Patagonia unravelled by the seismic stratigraphy of Laguna Potrok Aike. *Sedimentology* 56: 873-892.

Ariztegui D, Gilli A, Anselmetti FS, et al. (2010) Lake-level changes in central Patagonia (Argentina): crossing environmental thresholds for Lateglacial and Holocene human occupation. *Journal of Quaternary Science* 25: 1092-1099.

Battarbee EW. (1986) Diatom analysis. In: Berglund BE (ed) *Handbook of Holocene Palaeoecology and Palaeohydrology*. New York: J. Wiley & Sons, 527-570.

Bentley MJ, Hodgson DA, Smith JA, et al. (2009) Mechanisms of Holocene palaeoenvironmental change in the Antarctic Peninsula region. *The Holocene* 19: 51-69.

Berger A and Loutre MF. (1991) Insolation Values for the Climate of the Last 10,000,000 Years. *Quaternary Science Reviews* 10: 297-317.

Berman AL, Silvestri G and Compagnucci R. (2012) Eastern Patagonia Seasonal Precipitation: Influence of Southern Hemisphere Circulation and Links with Subtropical South American Precipitation. *Journal of Climate* 25: 6781-6795.

Bertrand S, Lange CB, Pantoja S, et al. (2017) Postglacial fluctuations of Cordillera Darwin glaciers (southernmost Patagonia) reconstructed from Almirantazgo fjord sediments. *Quaternary Science Reviews* 177: 265-275.

Bitschene PR and Fernandez MI. (1995) Volcanology and petrology of fallout ashes from the August 1991 eruption of the Hudson volcano (Patagonian Andes). In: Bitschene PR and Mendia J (eds) *The August 1991 eruption of the Hudson volcano (Patagonian Andes): a thousand days after*. Göttingen: Cuvillier, 27-54.

Björck S, Rundgren M, Ljung K, et al. (2012) Multi-proxy analyses of a peat bog on Isla de los Estados, easternmost Tierra del Fuego: a unique record of the variable Southern Hemisphere Westerlies since the last deglaciation. *Quaternary Science Reviews* 42: 1-14.

Blaauw M. (2010) Methods and code for ‘classical’ age-modelling of radiocarbon sequences. *Quaternary Geochronology* 5: 512-518.

Boës X and Fagel N. (2008) Relationships between southern Chilean varved lake sediments, precipitation and ENSO for the last 600 years. *Journal of Paleolimnology* 39: 237-252.

Braig E, Mayr C, Kirchner G, et al. (2013) Fifty years of eutrophication and lake restoration reflected in sedimentary carbon and nitrogen isotopes of a small, hardwater lake (South Germany). *Journal of Limnology* 72: 262-279.

Cartwright A, Quade J, Stine S, et al. (2011) Chronostratigraphy and lake-level changes of Laguna Cari-Laufquen, Rio Negro, Argentina. *Quaternary Research* 76: 430-440.

Clement AC, Seager R and Cane MA. (1999) Orbital controls on the El Nino/Southern Oscillation and the tropical climate. *Paleoceanography* 14: 441-456.

Clement AC, Seager R and Cane MA. (2000) Suppression of El Nino during the mid-Holocene by changes in the Earth's orbit. *Paleoceanography* 15: 731-737.

Cohen AS. (2003) *Paleolimnology. The History and Evolution of Lake Systems,* Oxford: Oxford University Press.

Corbella H. (2002) El campo volcano-tectónico de Pali Aike. In: Haller M (ed) *Geología y Recursos Naturales de Santa Cruz. Asociación Geológica Argentina.* Buenos Aires, 285-302.

Coronato A, Fanning P, Salemme M, et al. (2011) Aeolian sequence and the archaeological record in the fuegian steppe, Argentina. *Quaternary International* 245: 122-135.

Croudace IW and Rothwell RG. (2015) Future Developments and Innovations in High-Resolution Core Scanning. *Micro-Xrf Studies of Sediment Cores: Applications of a Non-Destructive Tool for the Environmental Sciences* 17: 627-647.

D'Orazio M, Agostini S, Mazzarini F, et al. (2000) The Pali Aike Volcanic Field, Patagonia: slab-window magmatism near the tip of South America. *Tectonophysics* 321: 407-427.

Dean WE. (1974) Determination of Carbonate and Organic-Matter in Calcareous Sediments and Sedimentary-Rocks by Loss on Ignition - Comparison with Other Methods. *Journal of Sedimentary Petrology* 44: 242-248.

Dearing J. (1994) *Environmental magnetic susceptibility: using the Bartington MS2 system,* Keniloworth: Chi Publishing.

Del Carlo P, Di Roberto A, D'Orazio M, et al. (2018) Late Glacial-Holocene tephra from southern Patagonia and Tierra del Fuego (Argentina, Chile): A complete textural and geochemical fingerprinting for distal correlations in the Southern Hemisphere. *Quaternary Science Reviews* 195: 153-170.

Domack E, Leventer A, Dunbar R, et al. (2001) Chronology of the Palmer Deep site, Antarctic Peninsula: a Holocene palaeoenvironmental reference for the circum-Antarctic. *The Holocene* 11: 1-9.

Echeverria ME, Bamonte FP, Marcos MA, et al. (2017) Palaeohydric balance variations in eastern Andean environments in southern Patagonia (48°–52.5° S): Major trends and forcings during the last ca. 8000 cal yrs BP. *Review of Palaeobotany and Palynology* 246: 242-250.

Faegri K and Iversen J. (1989) *Textbook of pollen analysis,* Chichester: John Wiley & Sons.

Fey M, Korr C, Maidana NI, et al. (2009) Palaeoenvironmental changes during the last 1600 years inferred from the sediment record of a cirque lake in southern Patagonia (Laguna Las Vizcachas, Argentina). *Palaeogeography, Palaeoclimatology, Palaeoecology* 281: 363-375.

Fischer H, Schmitt J, Luthi D, et al. (2010) The role of Southern Ocean processes in orbital and millennial CO_2 variations - A synthesis. *Quaternary Science Reviews* 29: 193-205.

Fletcher MS and Moreno PI. (2011) Zonally symmetric changes in the strength and position of the Southern Westerlies drove atmospheric CO_2 variations over the past 14 k.y. *Geology* 39: 419-422.

Fletcher MS and Moreno PI. (2012) Have the Southern Westerlies changed in a zonally symmetric manner over the last 14,000 years? A hemisphere-wide take on a controversial problem. *Quaternary International* 276: 299-299.

Fontana SL and Bennett KD. (2012) Postglacial vegetation dynamics of western Tierra del Fuego. *The Holocene* 22: 1337-1350.

Fontijn K, Lachowycz SM, Rawson H, et al. (2014) Late Quaternary tephrostratigraphy of southern Chile and Argentina. *Quaternary Science Reviews* 89: 70-84.

Fontijn K, Rawson H, Van Daele M, et al. (2016) Synchronisation of sedimentary records using tephra: A postglacial tephrochronological model for the Chilean Lake District. *Quaternary Science Reviews* 137: 234-254.

Ganopolski A, Kubatzki C, Claussen M, et al. (1998) The influence of vegetation-atmosphere-ocean interaction on climate during the mid-Holocene. *Science* 280: 1916-1919.

Garreaud R, Lopez P, Minvielle M, et al. (2013) Large-Scale Control on the Patagonian Climate. *Journal of Climate* 26: 215-230.

Gassmann MI and Pérez CF. (2006) Trajectories associated to regional and extra-regional pollen transport in the southeast of Buenos Aires province, Mar del Plata (Argentina). *International Journal of Biometeorology* 50: 280.

Gebhardt AC, Ohlendorf C, Niessen F, et al. (2012) Seismic evidence of up to 200 m lake-level change in Southern Patagonia since Marine Isotope Stage 4. *Sedimentology* 59: 1087-1100.

Grimm EC. (1987) Coniss - a Fortran-77 Program for Stratigraphically Constrained Cluster-Analysis by the Method of Incremental Sum of Squares. *Computers & Geosciences* 13: 13-35.

Haberzettl T, Corbella H, Fey M, et al. (2007) Lateglacial and Holocene wet-dry cycles in southern Patagonia: chronology, sedimentology and geochemistry of a lacustrine record from Laguna Potrok Aike, Argentina. *The Holocene* 17: 297-310.

Haberzettl T, Fey M, Lücke A, et al. (2005) Climatically induced lake level changes during the last two millennia as reflected in sediments of Laguna Potrok Aike, southern Patagonia (Santa Cruz, Argentina). *Journal of Paleolimnology* 33: 283-302.

Haberzettl T, Kück B, Wulf S, et al. (2008) Hydrological variability in southeastern Patagonia and explosive volcanic activity in the southern Andean Cordillera during Oxygen Isotope Stage 3 and the Holocene inferred from lake sediments of Laguna Potrok Aike, Argentina. *Palaeogeography, Palaeoclimatology, Palaeoecology* 259: 213-229.

Hahn A, Kliem P, Ohlendorf C, et al. (2013) Climate induced changes as registered in inorganic and organic sediment components from Laguna Potrok Aike (Argentina) during the past 51 ka. *Quaternary Science Reviews* 71: 154-166.

Hajdas I, Bonani G, Zolitschka B, et al. (1998) ^{14}C ages of terrestrial macrofossils from Lago Grande di Monticchio (Italy). *Radiocarbon* 40: 803-807.

Hakala A. (2004) Meromixis as a part of lake evolution - observations and a revised classification of true meromictic lakes in Finland. *Boreal Environment Research* 9: 37-53.

Helama S, Jones PD and Briffa KR. (2017) Dark Ages Cold Period: A literature review and directions for future research. *The Holocene* 27: 1600-1606.

Heusser CJ. (1971) *Pollen and spores of Chile,* Tucson: The University of Arizona Press.

Heyng AM, Mayr C, Lücke A, et al. (2012) Environmental changes in northern New Zealand since the Middle Holocene inferred from stable isotope records (δ^{15}N, δ^{13}C) of Lake Pupuke. *Journal of Paleolimnology* 48: 351-366.

Hodell DA, Kanfoush SL, Shemesh A, et al. (2001) Abrupt cooling of Antarctic surface waters and sea ice expansion in the South Atlantic sector of the Southern Ocean at 5000 cal yr B.P. *Quaternary Research* 56: 191-198.

Hogg AG, Hua Q, Blackwell PG, et al. (2013) Shcal13 Southern Hemisphere Calibration, 0-50,000 Years cal BP. *Radiocarbon* 55: 1889-1903.

Hollander DJ and Smith MA. (2001) Microbially mediated carbon cycling as a control on the δ^{13}C of sedimentary carbon in eutrophic Lake Mendota (USA): New models for interpreting isotopic excursions in the sedimentary record. *Geochimica et Cosmochimica Acta* 65: 4321-4337.

Hua Q, Barbetti M and Rakowski AZ. (2013) Atmospheric Radiocarbon for the Period 1950-2010. *Radiocarbon* 55: 2059-2072.

Hunt JB and Hill PG. (1996) An inter-laboratory comparison of the electron probe microanalysis of glass geochemistry. *Quaternary International* 34-36: 229-241.

Jones JM and Widmann M. (2004) Atmospheric science - Early peak in Antarctic oscillation index. *Nature* 432: 290-291.

Kang SM, Polvani LM, Fyfe JC, et al. (2011) Impact of Polar Ozone Depletion on Subtropical Precipitation. *Science* 332: 951-954.

Kaplan MR, Schaefer JM, Strelin JA, et al. (2016) Patagonian and southern South Atlantic view of Holocene climate. *Quaternary Science Reviews* 141: 112-125.

Kastner S, Enters D, Ohlendorf C, et al. (2010) Reconstructing 2000 years of hydrological variation derived from laminated proglacial sediments of Lago del Desierto at the eastern margin of the South Patagonian Ice Field, Argentina. *Global and Planetary Change* 72: 201-214.

Kilian R, Hohner M, Biester H, et al. (2003) Holocene peat and lake sediment tephra record from the southernmost Chilean Andes (53-55°S). *Revista Geológica de Chile* 30: 23-37.

Kilian R and Lamy F. (2012) A review of Glacial and Holocene paleoclimate records from southernmost Patagonia (49-55 degrees S). *Quaternary Science Reviews* 53: 1-23.

Kliem P, Buylaert JP, Hahn A, et al. (2013) Magnitude, geomorphologic response and climate links of lake level oscillations at Laguna Potrok Aike, Patagonian steppe (Argentina). *Quaternary Science Reviews* 71: 131-146.

Kohfeld KE, Graham RM, de Boer AM, et al. (2013) Southern Hemisphere westerly wind changes during the Last Glacial Maximum: paleo-data synthesis. *Quaternary Science Reviews* 68: 76-95.

Krammer K and Lange-Bertalot H. (1986) Bacillariophyceae 1. Teil: Naviculaceae. In: Ettl H, Gerloff J, Heynig H, et al. (eds) *Süßwasserflora von Mitteleuropa.* Jena: G. Fischer, 1-876.

Krammer K and Lange-Bertalot H. (1988) Bacillariophyceae 2. Teil: Bacillariaceae, Epithemiaceae, Surirellaceae. In: Ettl H, Gerloff J, Heynig H, et al. (eds) *Süßwasserflora von Mitteleuropa.* Jena: G. Fischer, 1-596.

Krammer K and Lange-Bertalot H. (1991a) Bacillariophyceae 3. Teil: Centrales, Fragilariaceae, Eunotiaceae. Unter Mitarbeit von H. Håkansson und M. Nörpel. In: Ettl H, Gerloff J, Heynig H, et al. (eds) *Süßwasserflora von Mitteleuropa.* Stuttgart, Jena: G. Fischer, 1-576.

Krammer K and Lange-Bertalot H. (1991b) Bacillariophyceae 4. Teil: Achnanthaceae, Kritische Ergänzungen zu Navicula (Lineolatae) und Gomphonema. In: Ettl H, Gärtner G, Gerloff J, et al. (eds) *Süßwasserflora von Mitteleuropa.* Stuttgart, Jena: G. Fischer, 1-437.

Kuehn SC, Froese DG, Shane PAR, et al. (2011) The INTAV intercomparison of electron-beam microanalysis of glass by tephrochronology laboratories: Results and recommendations. *Quaternary International* 246: 19-47.

Lamy F, Hebbeln D and Wefer G. (1999) High-Resolution Marine Record of Climatic Change in Mid-latitude Chile during the Last 28,000 Years Based on Terrigenous Sediment Parameters. *Quaternary Research* 51: 83-93.

Lamy F, Kilian R, Arz HW, et al. (2010) Holocene changes in the position and intensity of the southern westerly wind belt. *Nature Geoscience* 3: 695-699.

Le Bas MJ, Le Maitre RW, Streckeisen A, et al. (1986) A chemical classification of volcanic rocks based on the Total Alkali-Silica diagram. *Journal of Petrology* 27: 745-750.

Le Quere C, Rodenbeck C, Buitenhuis ET, et al. (2007) Saturation of the Southern Ocean CO_2 sink due to recent climate change. *Science* 316: 1735-1738.

León RJC, Bran D, Collantes M, et al. (1998) Grandes unidades de vegetación de la Patagonia extra andina. *Ecologia Austral* 8: 125-144.

Ljung K, Björk S, Hammarlund D, et al. (2006) Late Holocene multi-proxy records of environmental change on the South Atlantic island Tristan da Cunha. *Palaeogeography, Palaeoclimatology, Palaeoecology* 241: 539-560.

Lovenduski NS, Fay AR and McKinley GA. (2015) Observing multidecadal trends in Southern Ocean CO_2 uptake: What can we learn from an ocean model? *Global Biogeochemical Cycles* 29: 416-426.

Lovenduski NS, Gruber N and Doney SC. (2008) Toward a mechanistic understanding of the decadal trends in the Southern Ocean carbon sink. *Global Biogeochemical Cycles* 22.

Mancini MV, Prieto AR, Paez MM, et al. (2008) Late Quaternary vegetation and climate of Patagonia. In: Rabassa J (ed) *Late Cenozoic of Patagonia and Tierra del Fuego.* 351-367.

Mansilla CA, McCulloch RD and Morello F. (2016) Palaeoenvironmental change in Southern Patagonia during the Lateglacial and Holocene: Implications for forest refugia and climate reconstructions. *Palaeogeography Palaeoclimatology Palaeoecology* 447: 1-11.

Markgraf V. (1998) Past climates of South America. In: Hobbs JE, Lindesay JA and Bridgman HA (eds) *Climates of the southern continents: present, past and future.* Chichester: Wiley, 249-264.

Markgraf V and D'Antoni HL. (1978) *Pollen flora of Argentina,* Tucson: The University of Arizona Press.

Markgraf V and Huber UM. (2010) Late and postglacial vegetation and fire history in Southern Patagonia and Tierra del Fuego. *Palaeogeography Palaeoclimatology Palaeoecology* 297: 351-366.

Massaferro J and Larocque-Tobler I. (2013) Using a newly developed chironomid transfer function for reconstructing mean annual air temperature at Lake Potrok Aike, Patagonia, Argentina. *Ecological Indicators* 24: 201-210.

Mayr C, Fey M, Haberzettl T, et al. (2005) Palaeoenvironmental changes in southern Patagonia during the last millennium recorded in lake sediments from Laguna Azul (Argentina). *Palaeogeography, Palaeoclimatology, Palaeoecology* 228: 203-227.

Mayr C, Lücke A, Stichler W, et al. (2007a) Precipitation origin and evaporation of lakes in semi-arid Patagonia (Argentina) inferred from stable isotopes (δ^{18}O, δ^{2}H). *Journal of Hydrology* 334: 53-63.

Mayr C, Wille M, Haberzettl T, et al. (2007b) Holocene variability of the Southern Hemisphere westerlies in Argentinean Patagonia (52°S). *Quaternary Science Reviews* 26: 579-584.

Messyasz B, Maidana N, Mayr C, et al. (2007) Summer phytoplankton and the hydrochemistry of the crater lake Laguna Azul (Santa Cruz, Argentina). *Oceanological and Hydrobiological Studies - International Journal of Oceanography and Hydrobiology* 36: 95-105.

Meyers PA. (2003) Applications of organic geochemistry to paleolimnological reconstructions: a summary of examples from the Laurentian Great Lakes. *Organic Geochemistry* 34: 261-289.

Meyers PA and Lallier-Verges E. (1999) Lacustrine sedimentary organic matter records of Late Quaternary paleoclimates. *Journal of Paleolimnology* 21: 345-372.

Moreno PI, Francois JP, Moy CM, et al. (2010) Covariability of the Southern Westerlies and atmospheric CO_2 during the Holocene. *Geology* 38: 727-730.

Moreno PI, François JP, Villa-Martínez RP, et al. (2009) Millennial-scale variability in Southern Hemisphere westerly wind activity over the last 5000 years in SW Patagonia. *Quaternary Science Reviews* 28: 25-38.

Moreno PI and Videla J. (2016) Centennial and millennial-scale hydroclimate changes in northwestern Patagonia since 16,000 yr BP. *Quaternary Science Reviews* 149: 326-337.

Moreno PI, Vilanova I, Villa-Martinez R, et al. (2014) Southern Annular Mode-like changes in southwestern Patagonia at centennial timescales over the last three millennia. *Nature Communications* 5.

Moy CM, Seltzer GO, Rodbell DT, et al. (2002) Variability of El Nino/Southern Oscillation activity at millennial timescales during the Holocene epoch. *Nature* 420: 162-165.

Müller PJ and Schneider R. (1993) An automated leaching method for the determination of opal in sediments and particulate matter. *Deep-Sea Research* 40: 425-444.

Naranjo JA and Stern CR. (1998) Holocene explosive activity of Hudson Volcano, southern Andes. *Bulletin of Volcanology* 59: 291-306.

Nemeth K and Kereszturi G. (2015) Monogenetic volcanism: personal views and discussion. *International Journal of Earth Sciences* 104: 2131-2146.

Nowaczyk NR. (2001) Logging of magnetic susceptibility. In: Last WM and Smol JP (eds) *Tracking environmental changes using lake sediments. Volume 1: Basin analysis, coring, and chronological techniques.* Dordrecht, The Netherlands: Kluwer Academic Publishers, 155-170.

Ohlendorf C, Fey M, Gebhardt C, et al. (2013) Mechanisms of lake-level change at Laguna Potrok Aike (Argentina) - insights from hydrological balance calculations. *Quaternary Science Reviews* 71: 27-45.

Ohlendorf C, Fey M, Massaferro J, et al. (2014) Late Holocene hydrology inferred from lacustrine sediments of Laguna Cháltel (southeastern Argentina). *Palaeogeography Palaeoclimatology Palaeoecology* 411: 229-248.

Ohlendorf C, Gebhardt C, Hahn A, et al. (2011) The PASADO core processing strategy - A proposed new protocol for sediment core treatment in multidisciplinary lake drilling projects. *Sedimentary Geology* 239: 104-115.

Oliva G, González L, Rial P, et al. (2001) El ambiente en la Patagonia Austral. In: Borrelli P and Oliva G (eds) *Ganadería ovina sustentable en la Patagonia Austral - tecnología de manejo extensivo.* Río Gallegos, Santa Cruz, Argentina: INTA Centro Regional Patagonia Sur, 19-82.

Owens MJ, Lockwood M, Hawkins E, et al. (2017) The Maunder minimum and the Little Ice Age: an update from recent reconstructions and climate simulations. *Journal of Space Weather and Space Climate* 7: 10.

Pasquier-Cardin A, Allard P, Ferreira T, et al. (1999) Magma-derived CO_2 emissions recorded in ^{14}C and ^{13}C content of plants growing in Furnas caldera, Azores. *Journal of Volcanology and Geothermal Research* 92: 195-207.

Pirrung M, Büchel G, Lorenz V, et al. (2008) Post-eruptive development of the Ukinrek East Maar since its eruption in 1977 A.D. in the periglacial area of south-west Alaska. *Sedimentology* 55: 305-334.

Porter SC. (2000) Onset of Neoglaciation in the Southern Hemisphere. *Journal of Quaternary Science* 15: 395-408.

Quade J and Kaplan MR. (2017) Lake-level stratigraphy and geochronology revisited at Lago (Lake) Cardiel, Argentina, and changes in the Southern Hemispheric Westerlies over the last 25 ka. *Quaternary Science Reviews* 177: 173-188.

Recasens C, Ariztegui D, Gebhardt C, et al. (2012) New insights into paleoenvironmental changes in Laguna Potrok Aike, southern Patagonia, since the Late Pleistocene: The PASADO multiproxy record. *The Holocene* 22: 1323-1335.

Rumrich U, Lange-Bertalot H and Rumrich M. (2000) Diatoms of the Andes. From Venezuela to Patagonia/Tierra del Fuego and two additional contributions. *Iconographia Diatomologica* 9: 1-673.

Sandweiss DH, Richardson JB, Reitz EJ, et al. (1996) Geoarchaeological evidence from Peru for a 5000 years BP onset of El Nino. *Science* 273: 1531-1533.

Schäbitz F, Wille M, Francois JP, et al. (2013) Reconstruction of palaeoprecipitation based on pollen transfer functions - the record of the last 16 ka from Laguna Potrok Aike, southern Patagonia. *Quaternary Science Reviews* 71: 175-190.

Schimpf D, Kilian R, Kronz A, et al. (2011) The significance of chemical, isotopic, and detrital components in three coeval stalagmites from the superhumid southernmost Andes (53 degrees S) as high-resolution palaeo-climate proxies. *Quaternary Science Reviews* 30: 443-459.

Schindler DW. (2009) Lakes as sentinels and integrators for the effects of climate change on watersheds, airsheds, and landscapes. *Limnology and Oceanography* 54: 2349-2358.

Shindell DT and Schmidt GA. (2004) Southern Hemisphere climate response to ozone changes and greenhouse gas increases. *Geophysical Research Letters* 31.

Simonsen R. (1987) *Atlas and catalogue of the diatom types of Friedrich Hustedt,* Berlin, Stuttgart: Gebr. Borntraeger.

Stern CR. (1990) Tephrochronology of southernmost Patagonia. *National Geographic Research* 6: 110-126.

Takahashi T, Sweeney C, Hales B, et al. (2012) The Changing Carbon Cycle in the Southern Ocean. *Oceanography* 25: 26-37.

Toggweiler JR, Russell JL and Carson SR. (2006) Midlatitude westerlies, atmospheric CO_2, and climate change during the ice ages. *Paleoceanography* 21.

Valero-Garces BL, Grosjean M, Schwalb A, et al. (1996) Limnogeology of Laguna Miscanti: Evidence for mid to late Holocene moisture changes in the Atacama Altiplano (Northern Chile). *Journal of Paleolimnology* 16: 1-21.

Van Daele M, Bertrand S, Meyer I, et al. (2016) Late Quaternary evolution of Lago Castor (Chile, 45.6 degrees S): Timing of the deglaciation in northern Patagonia and evolution of the southern westerlies during the last 17 kyr. *Quaternary Science Reviews* 133: 130-146.

Varma V, Prange M, Merkel U, et al. (2012) Holocene evolution of the Southern Hemisphere westerly winds in transient simulations with global climate models. *Clim. Past* 8: 391-402.

Villa-Martínez R and Moreno PI. (2007) Pollen evidence for variations in the southern margin of the westerly winds in SW Patagonia over the last 12,600 years. *Quaternary Research* 68: 400-409.

Villa-Martínez R, Villagrán C and Jenny B. (2003) The last 7500 cal yr B.P. of westerly rainfall in Central Chile inferred from a high-resolution pollen record from Laguna Aculeo (34°S). *Quaternary Research* 60: 284-293.

Villalba R, Lara A, Boninsegna JA, et al. (2003) Large-scale temperature changes across the southern Andes: 20th-century variations in the context of the past 400 years. *Climatic Change* 59: 177-232.

Waldmann N, Ariztegui D, Anselmetti FS, et al. (2010) Holocene climatic fluctuations and positioning of the Southern Hemisphere westerlies in Tierra del Fuego (54 degrees S), Patagonia. *Journal of Quaternary Science* 25: 1063-1075.

Wastegard S, Veres D, Kliem P, et al. (2013) Towards a late Quaternary tephrochronological framework for the southernmost part of South America - the Laguna Potrok Aike tephra record. *Quaternary Science Reviews* 71: 81-90.

Wille M, Maidana NI, Schäbitz F, et al. (2007) Vegetation and climate dynamics in southern South America: the microfossil record of Laguna Potrok Aike, Santa Cruz, Argentina. *Review of Palaeobotany and Palynology* 146: 234-246.

Zhang ZG, Han WX, Fang XM, et al. (2013) Late Miocene-Pleistocene aridification of Asian inland revealed by geochemical records of lacustrine-fan delta sediments from the western Tarim Basin, NW China. *Palaeogeography Palaeoclimatology Palaeoecology* 377: 52-61.

Zolitschka B, Anselmetti F, Ariztegui D, et al. (2013) Environment and climate of the last 51,000 years - new insights from the Potrok Aike maar lake Sediment Archive Drilling prOject (PASADO). *Quaternary Science Reviews* 71: 1-12.

Zolitschka B, Mingram J, Van der Gaast S, et al. (2001) Sediment Logging Techniques. In: Last WM and Smol JP (eds) *Tracking Environmental Change Using Lake Sediments. Volume 1: Basin Analysis, Coring, and Chronological Techniques.* Dordrecht: Kluwer Academic Press, 137-153.

Zolitschka B, Schäbitz F, Lücke A, et al. (2006) Crater lakes of the Pali Aike Volcanic Field as key sites for paleoclimatic and paleoecological reconstructions in southern Patagonia, Argentina. *Journal of South American Earth Sciences* 21: 294-309.

Table 1: AMS radiocarbon dates from Laguna Azul calibrated with Clam 2.2 (Blaauw, 2010) and the southern hemisphere calibration curve SHCal13 (Hogg et al., 2013). Modelled ages (n.d.: not determined) were obtained with the smoothed spline option of Clam 2.2. Samples above the first dashed line are not from the sediment core. Samples below the second dashed line are effectd by volcanogenic CO_2.

Core section or sample number	Core section depth (cm)	Mean composite sediment depth (cm)	Sample type	Lab. no.	Radiocarbon age (^{14}C BP ± 1σ)	$\delta^{13}C$ (‰)	Calibrated 2σ minimum age (cal. BP)	Calibrated 2σ maximum age (cal. BP)	Modelled age (cal. BP)
PAIS-48[a]	outcrop		aquatic macrophytes	Poz-5071	1325 ± 30	-10.5	1090	1290	n.d.
PAIS-45[a]	modern		*Potamogeton* sp.[b]	Poz-3574	104.9 ± 0.4[g]	-8.8	-6 to -8[h]	-57 to -61[h]	-53
AZU-02/4[a]	7.0-9.0	29.0	twig of *Berberis*[c]	Poz-3575	157 ± 0.5[g]	-25.4	-20	-10	-10
AZU 02/11[a]	64.0-66.0	46.0	charred plant remains[c]	Poz-8445	145 ± 30	-27.4	0	270	80
AZU 03/5[a]	42.0-45.0	53.3	charred plant remains[c]	Poz-8447	215 ± 35	-27.1	0	300	120
AZU 03/6-1	41.0-42.0	156.5	coarse fraction[d]	Poz-8501	900 ± 30	-20.3	690	900	850
AZU 03/6-1	63.0-64.0	178.5	TIC fraction[e]	Poz-8624	1360 ± 50	-14.2	1090	1310	1100
AZU 03/4-3	64.0-65,0	261.5	fish bones	Poz-6099	1700 ± 30	-18.4	1480	1700	1560
AZU 03/6-3	15.0-16.0	335.5	coarse fraction[d]	Poz-8553	1830 ± 50	-19,0	1590	1830	1760
AZU 03/6-3	88.5-89.3	408.9	fish bones	Poz-5976	2410 ± 40	-15,0	2320	2690	2340
AZU 03/6-4	43.0-44.0	464.5	fine fraction[f]	Poz-8449	2840 ± 35	-15.1	2790	3000	2970
AZU 03/6-5	12.5-13.5	538.0	fine fraction[f]	Poz-8554	4120 ± 40	-23.4	4440	4810	4670
AZU 03/6-5	12.5-13.5	538.0	coarse fraction[d]	Poz-8556	4270 ± 40	-27,0	4620	4860	4670
AZU 03/4-7	22.0-23.0	583.0	bulk sediment	Poz-5975	5280 ± 50	-23.7	5910	6130	6090
AZU 03/4-7	75.0-76.0	638.5	wood[c]	Poz-11585	7500 ± 80	-35.1	8050	8410	8220
AZU 03/4-7	80.0-81.0	643.5	*Ruppia* seed[b]	Poz-8446	16,710 ± 100[i]	-27.3	19,830	20,420	8420
AZU 03/4-8	31.0-32.0	694.5	TIC fraction[e]	Poz-8552	16,170 ± 110[i]	-0.3	19,140	19,780	10,460
AZU 03/4-8	62.2-63.2	725.7	fine fraction[f]	Poz-8500	26,420 ± 350[i]	-33.2	29,800	31,120	11,710
AZU 03/4-8	63.2-64.2	726.7	bulk sediment	Poz-5191	22,660 ± 190[i]	-32.9	26,460	27,370	11,750

[a] Mayr et al. (2005), modified

[b] aquatic macrophyte

[c] terrestrial plant remains

[d] coarse fraction (>100 µm) of bulk sediment

[e] total inorganic carbon fraction of bulk sediment

[f] fine fraction (<100 µm) of bulk sediment

[g] percent modern carbon (pMC)

[h] two probability ranges due to two well-defined intersections with the calibration curve

[i] date excluded from age-depth model: effected by volcanogenic CO_2

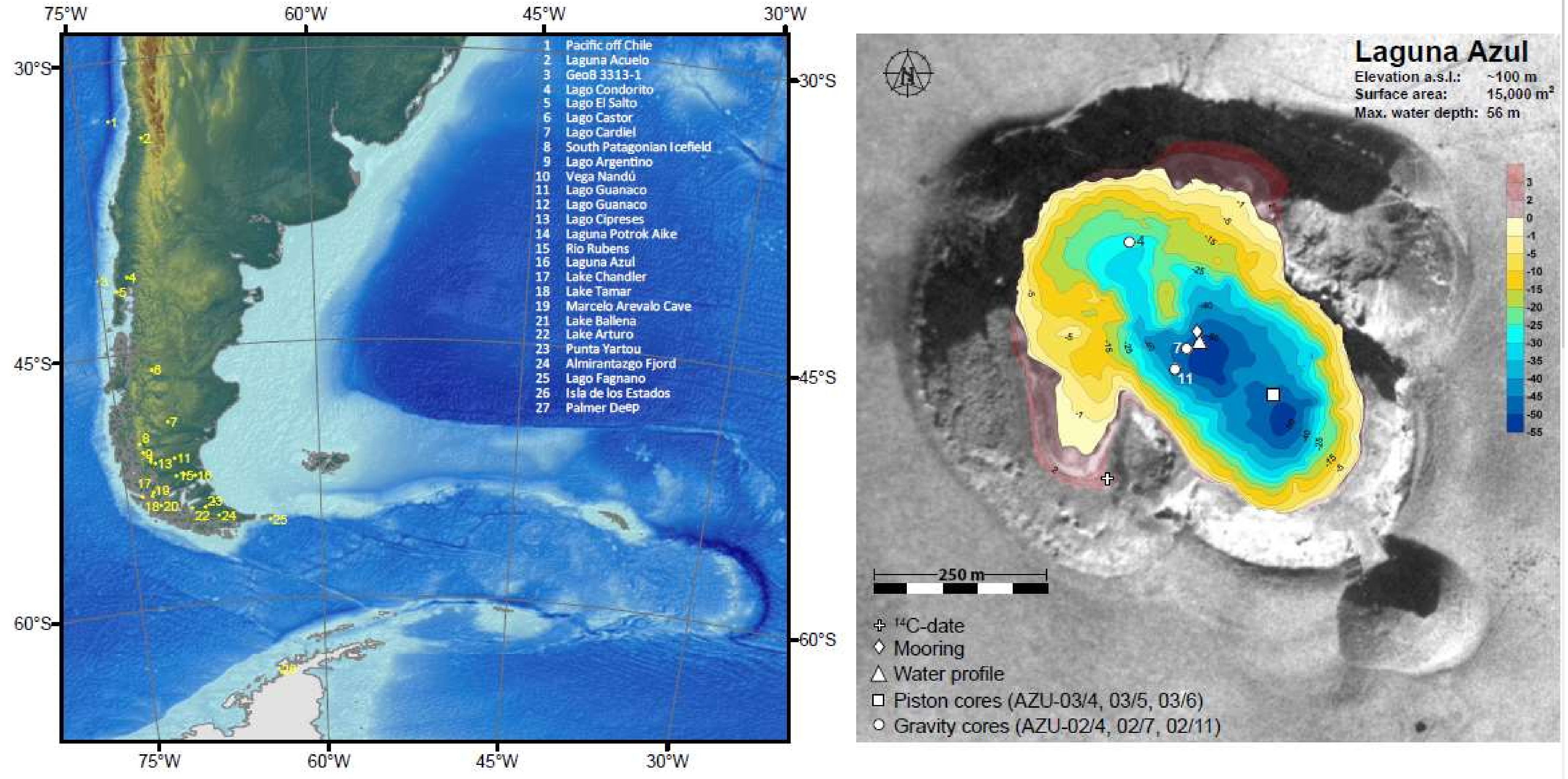
75°W
60°W
45°W
30°W
30°S
45°S
60°S
1 Pacific off Chile
2 Laguna Acuelo
3 GeoB 3313-1
4 Lago Condorito
5 Lago El Salto
6 Lago Castor
7 Lago Cardiel
8 South Patagonian Icefield
9 Lago Argentino
10 Vega Nandú
11 Lago Guanaco
12 Lago Guanaco
13 Lago Cipreses
14 Laguna Potrok Aike
15 Rio Rubens
16 Laguna Azul
17 Lake Chandler
18 Lake Tamar
19 Marcelo Arevalo Cave
21 Lake Ballena
22 Lake Arturo
23 Punta Yartou
24 Almirantazgo Fjord
25 Lago Fagnano
26 Isla de los Estados
27 Palmer Deep
N
Laguna Azul
Elevation a.s.l.: ~100 m
Surface area: 15,000 m²
Max. water depth: 56 m
3
2
0
-1
-5
-10
-15
-20
-25
-30
-35
-40
-45
-50
-55
4
7
11
250 m
✣ ¹⁴C-date
◇ Mooring
△ Water profile
□ Piston cores (AZU-03/4, 03/5, 03/6)
○ Gravity cores (AZU-02/4, 02/7, 02/11)

Fig. 1

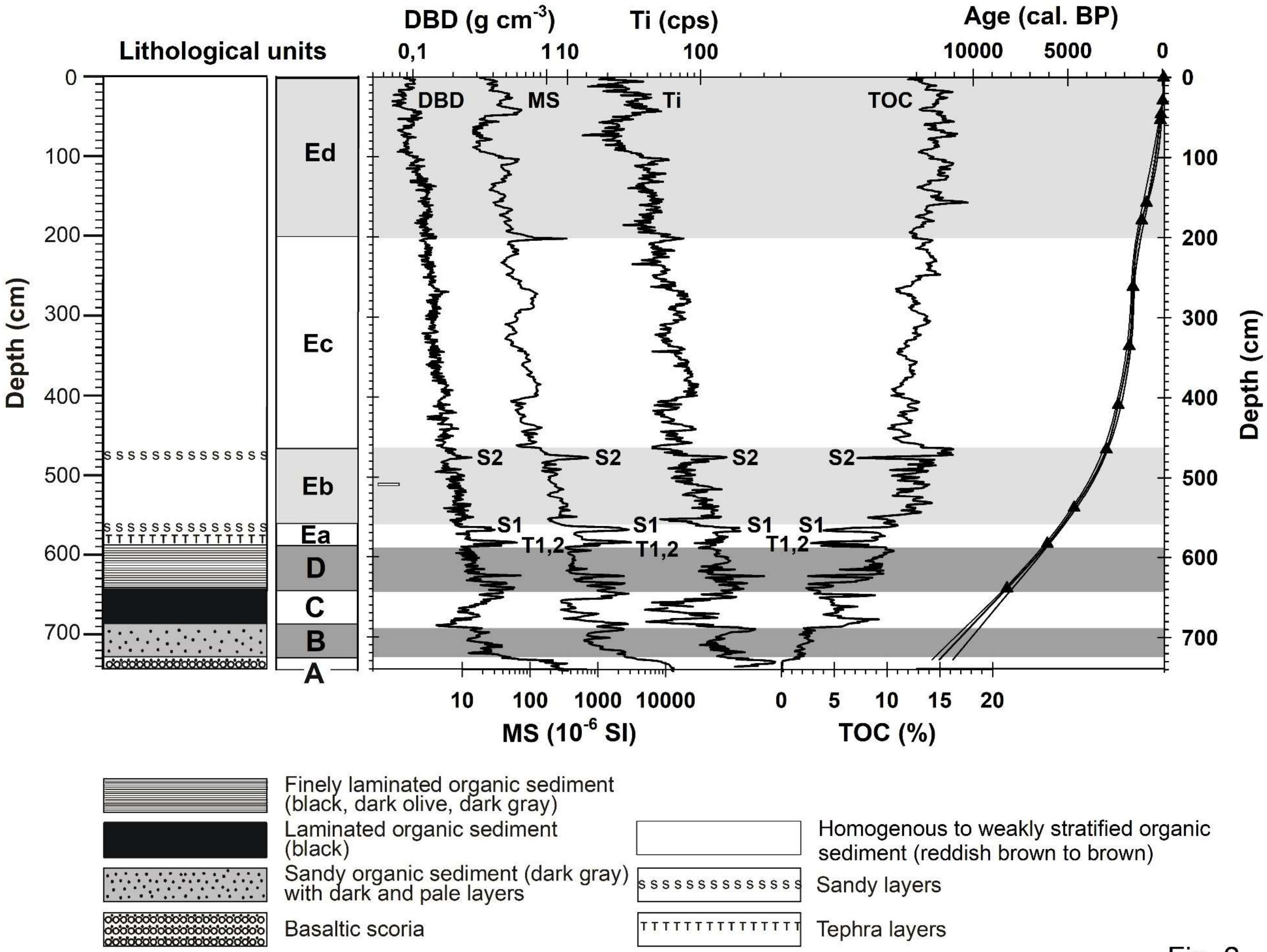
Lithological units
Depth (cm)
0
100
200
300
400
500
600
700
Ed
Ec
Eb
Ea
D
C
B
A
DBD (g cm^{-3})
0,1
1
Ti (cps)
10
100
Age (cal. BP)
10000
5000
0
DBD
MS
Ti
TOC
S2
S1
T1,2
10
100
1000
10000
MS (10^{-6} SI)
0
5
10
15
20
TOC (%)
Depth (cm)
Finely laminated organic sediment (black, dark olive, dark gray)
Laminated organic sediment (black)
Sandy organic sediment (dark gray) with dark and pale layers
Basaltic scoria
Homogenous to weakly stratified organic sediment (reddish brown to brown)
Sandy layers
Tephra layers

Fig. 2

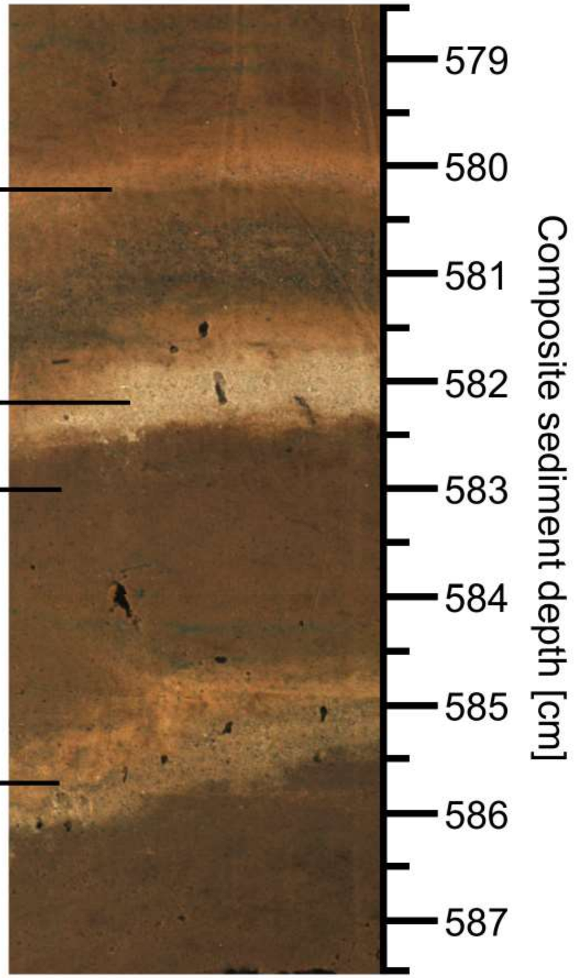

Reworked tephra

Tephra AZU-T2 (Mt. Burney)
Modelled age: 6050 cal. BP

Radiocarbon dating
5280 ±50 BP (6020 ±110 cal. BP)
Modelled age: 6090 cal. BP

Tephra AZU-T1 (NAVZ)
Modelled age: 6160 cal. BP

Fig. 3

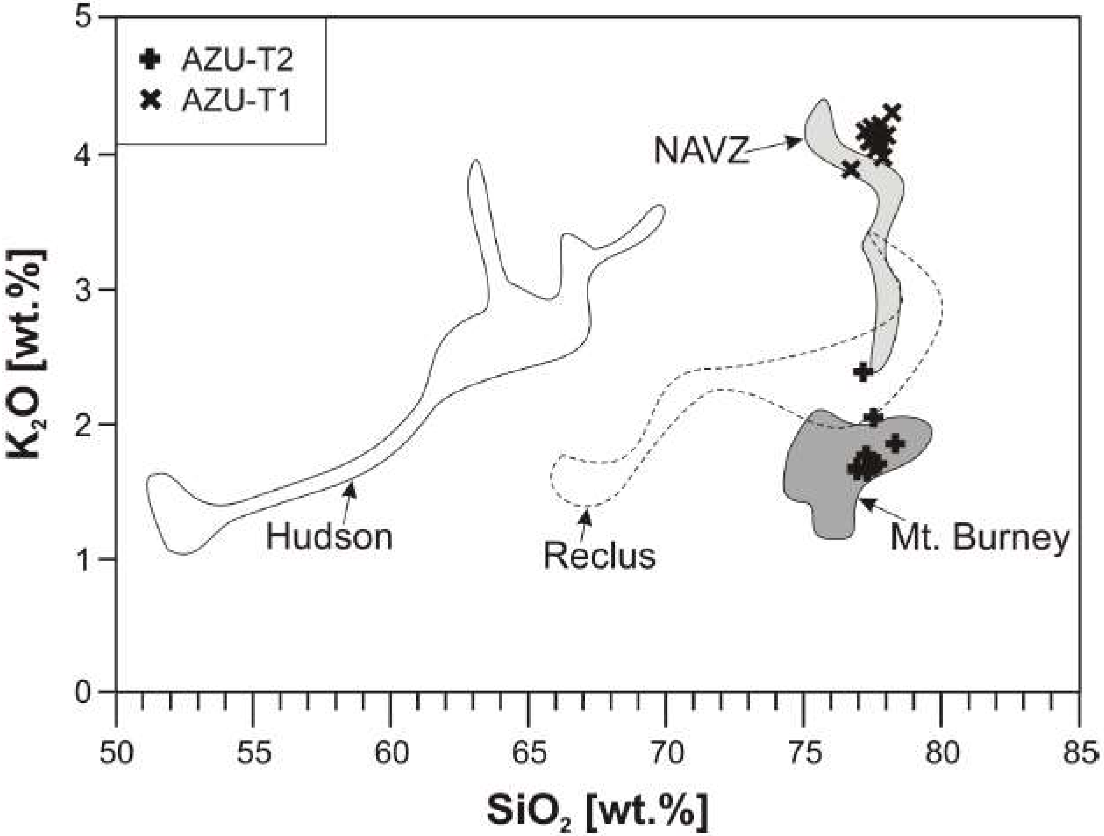
✚ AZU-T2
✖ AZU-T1
NAVZ
Hudson
Reclus
Mt. Burney
K_2O [wt.%]
SiO_2 [wt.%]
0
1
2
3
4
5
50
55
60
65
70
75
80
85

Fig. 4

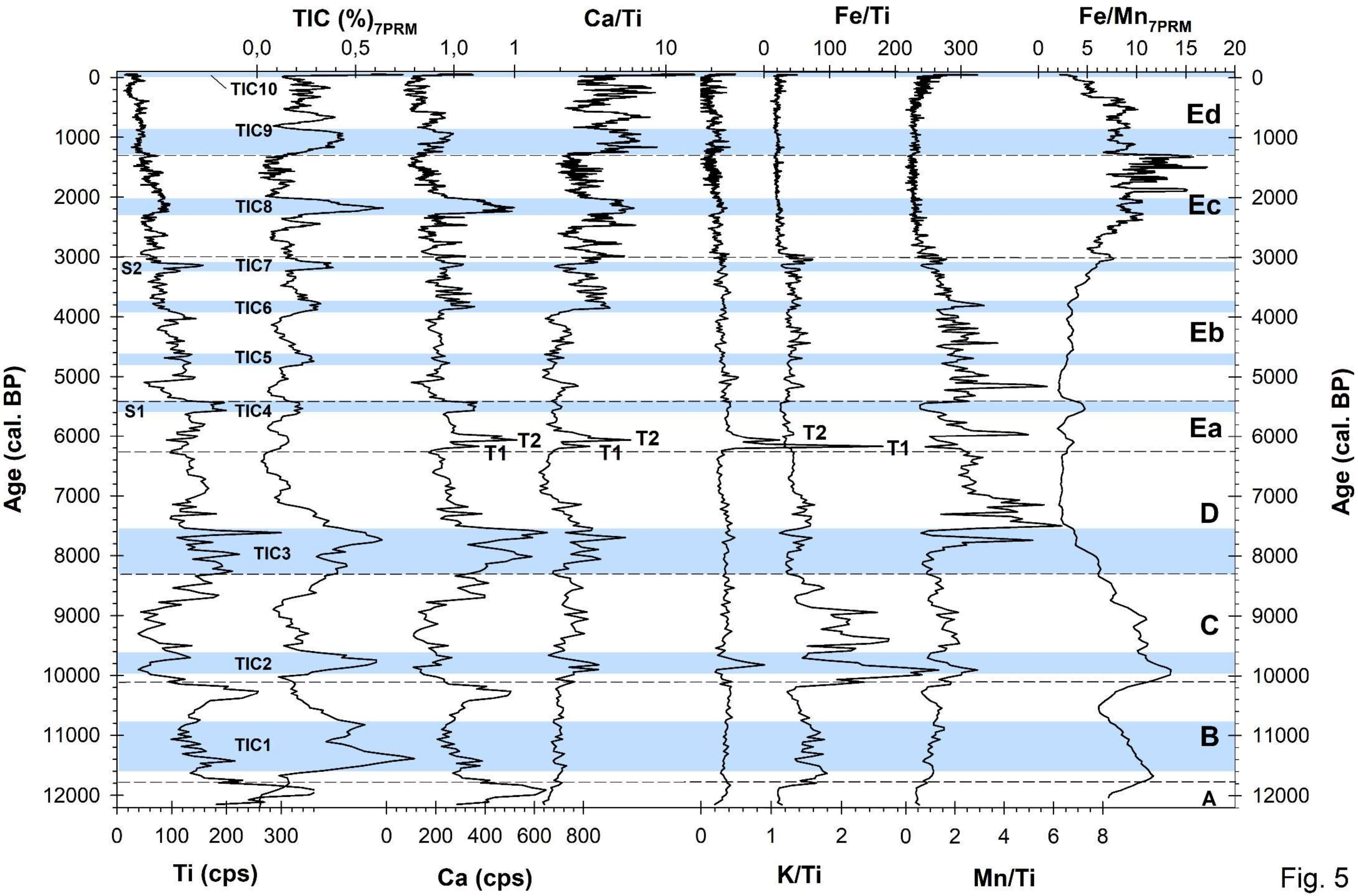
TIC (%)7PRM
0,0
0,5
1,0
Ca/Ti
1
10
Fe/Ti
0
100
200
300
Fe/Mn7PRM
0
5
10
15
20
Age (cal. BP)
0
1000
2000
3000
4000
5000
6000
7000
8000
9000
10000
11000
12000
TIC10
TIC9
TIC8
TIC7
TIC6
TIC5
TIC4
TIC3
TIC2
TIC1
S2
S1
T2
T1
T2
T1
T2
T1
Ed
Ec
Eb
Ea
D
C
B
A
0
100
200
300
0
200
400
600
800
0
1
2
0
2
4
6
8
Ti (cps)
Ca (cps)
K/Ti
Mn/Ti

Fig. 5

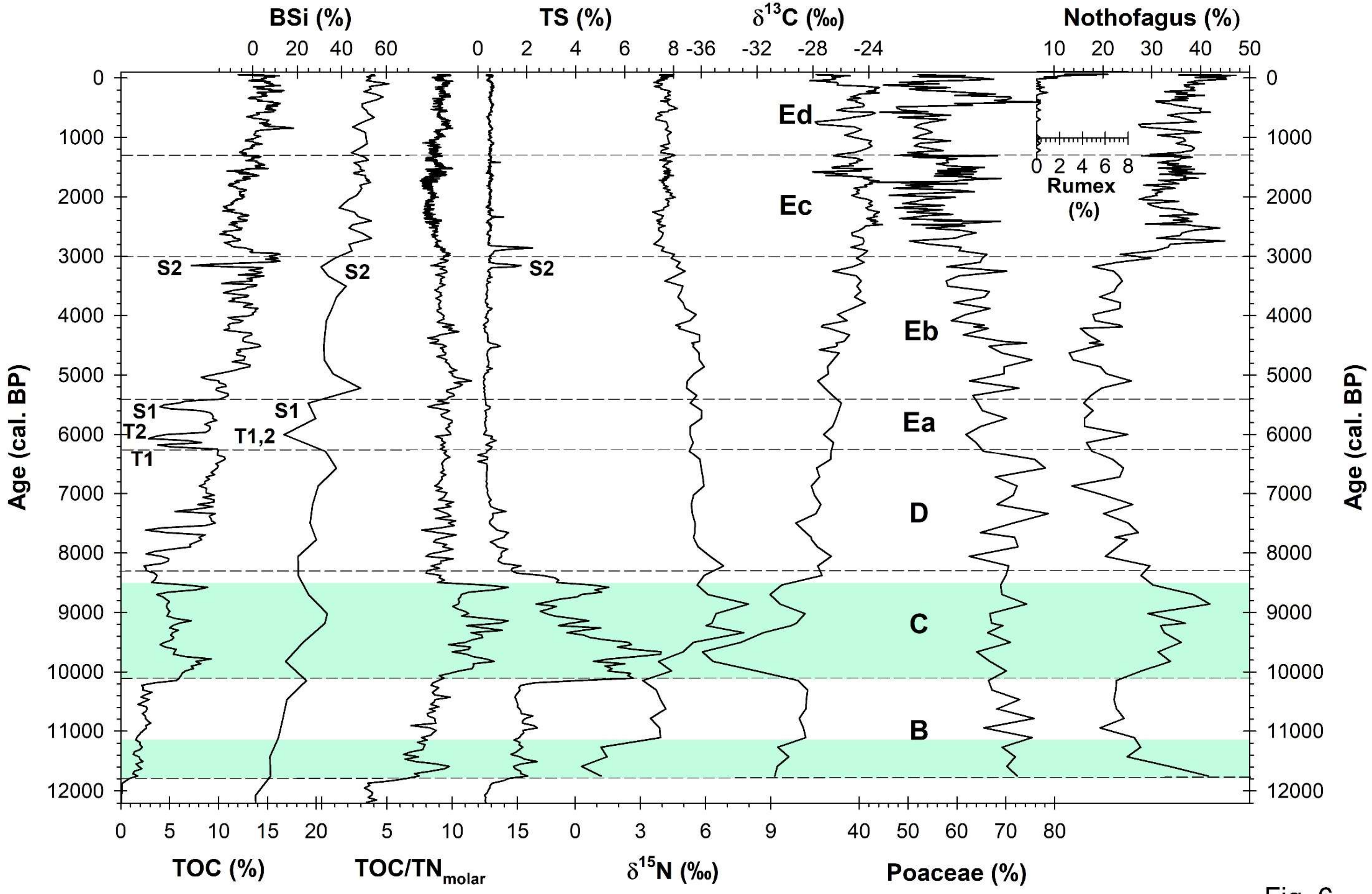
BSi (%)
0 20 40 60
TS (%)
0 2 4 6 8
δ^{13}C (‰)
-36 -32 -28 -24
Nothofagus (%)
10 20 30 40 50
Age (cal. BP)
0 1000 2000 3000 4000 5000 6000 7000 8000 9000 10000 11000 12000
Ed
Ec
Eb
Ea
D
C
B
S2
S2
S2
S1
S1
T2
T1
T1,2
0 2 4 6 8
Rumex (%)
0 5 10 15 20
TOC (%)
5 10 15
TOC/TN$_{molar}$
0 3 6 9
δ^{15}N (‰)
40 50 60 70 80
Poaceae (%)

Fig. 6

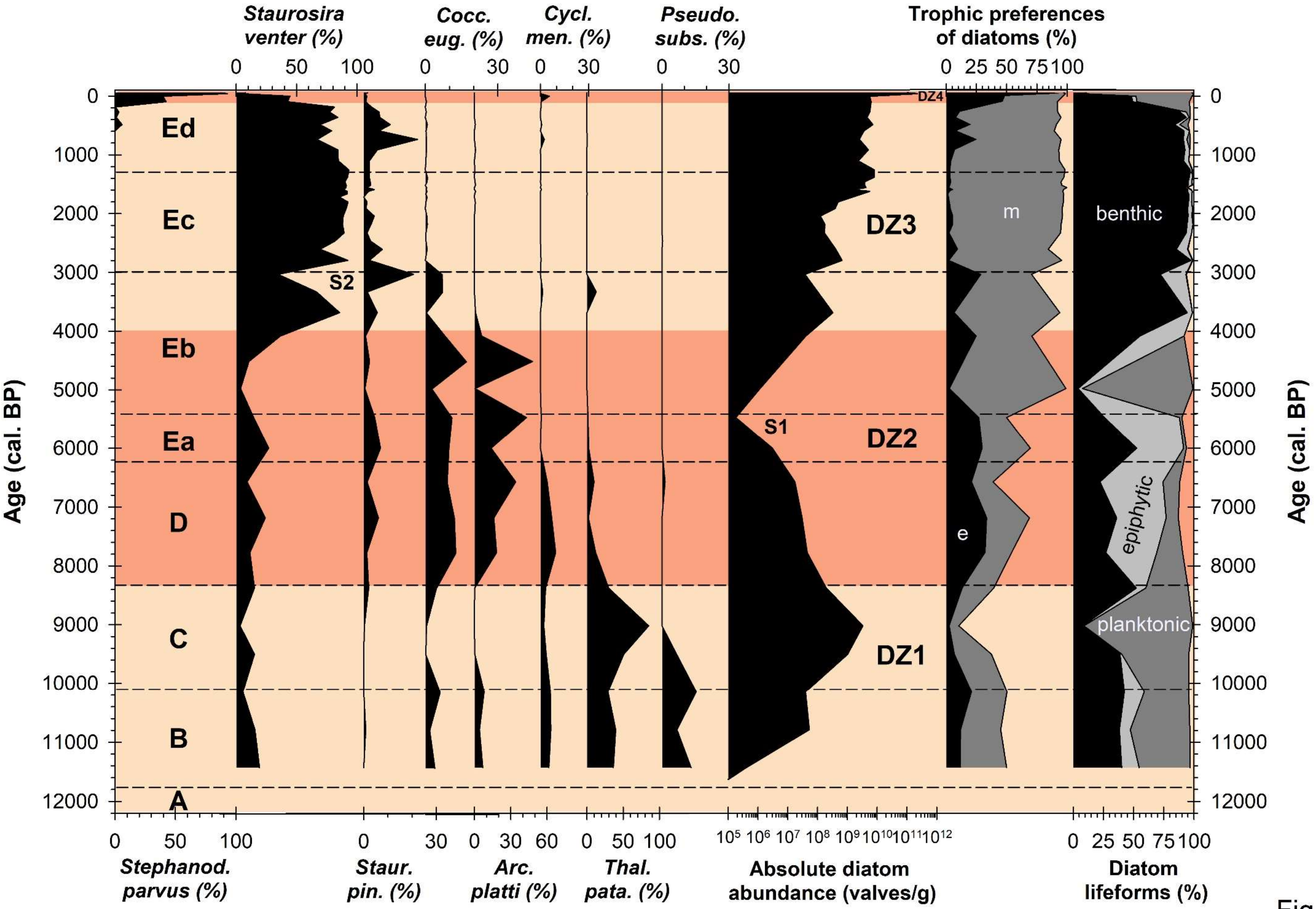

Staurosira venter (%)
Cocc. eug. (%)
Cycl. men. (%)
Pseudo. subs. (%)
Trophic preferences of diatoms (%)
0 50 100
0 30
0 30
0 30
0 25 50 75 100
Ed
Ec
Eb
Ea
D
C
B
A
S2
S1
DZ4
DZ3
DZ2
DZ1
m
e
benthic
epiphytic
planktonic
Age (cal. BP)
0 1000 2000 3000 4000 5000 6000 7000 8000 9000 10000 11000 12000
0 50 100
Stephanod. parvus (%)
0 30
Staur. pin. (%)
0 30 60
Arc. platti (%)
0 50 100
Thal. pata. (%)
10⁵ 10⁶ 10⁷ 10⁸ 10⁹ 10¹⁰ 10¹¹ 10¹²
Absolute diatom abundance (valves/g)
0 25 50 75 100
Diatom lifeforms (%)

Fig. 7

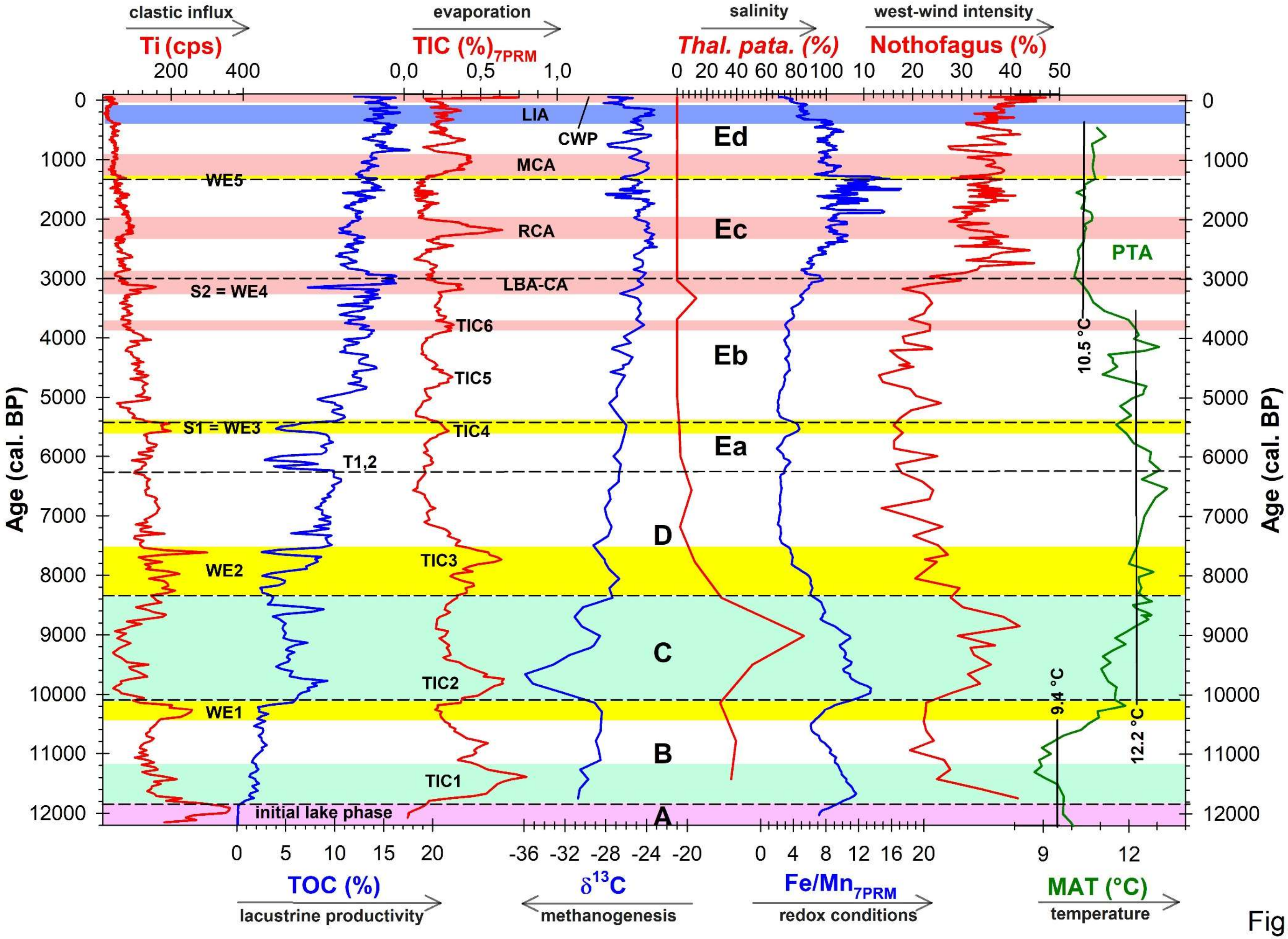
clastic influx
Ti (cps)
200 400
evaporation
TIC (%)7PRM
0,0 0,5 1,0
salinity
Thal. pata. (%)
0 20 40 60 80 100
west-wind intensity
Nothofagus (%)
10 20 30 40 50
Age (cal. BP)
0 1000 2000 3000 4000 5000 6000 7000 8000 9000 10000 11000 12000
LIA
CWP
MCA
WE5
RCA
LBA-CA
S2 = WE4
TIC6
TIC5
S1 = WE3
TIC4
T1,2
WE2
TIC3
TIC2
WE1
TIC1
initial lake phase
Ed
Ec
Eb
Ea
D
C
B
A
PTA
10.5 °C
9.4 °C
12.2 °C
0 5 10 15 20
TOC (%)
lacustrine productivity
-36 -32 -28 -24 -20
δ13C
methanogenesis
0 4 8 12 16 20
Fe/Mn7PRM
redox conditions
9 12
MAT (°C)
temperature

Fig. 8

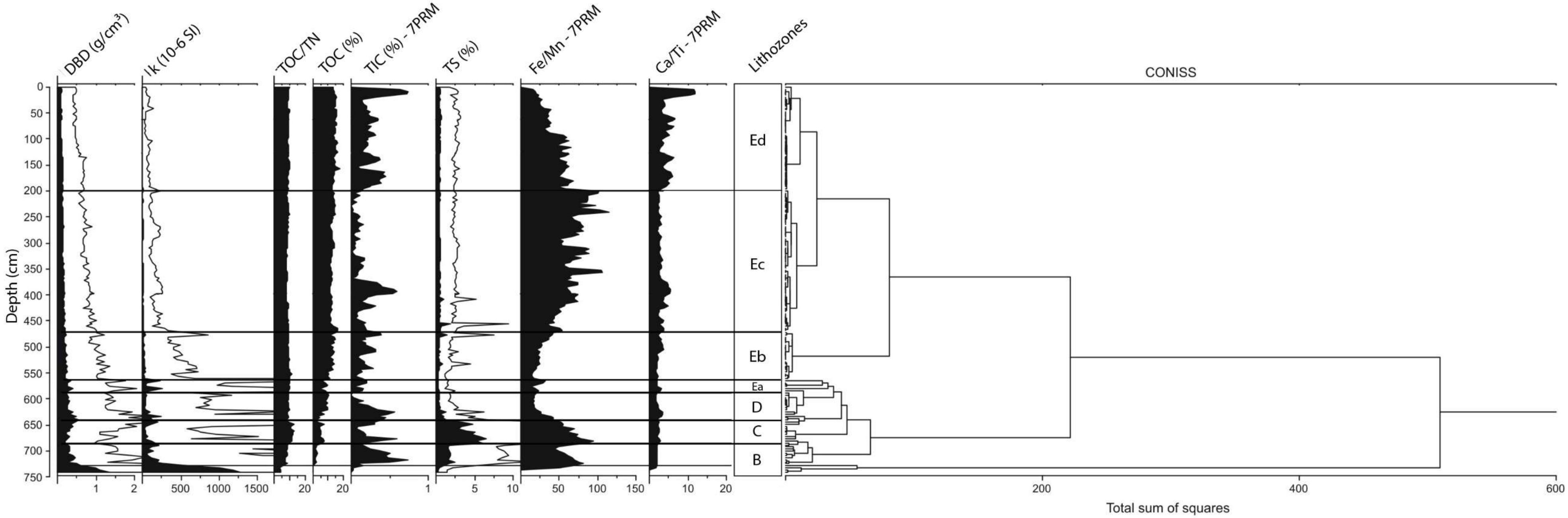
DBD (g/cm³)
Ik (10-6 SI)
TOC/TN
TOC (%)
TIC (%) - 7PRM
TS (%)
Fe/Mn - 7PRM
Ca/Ti - 7PRM
Lithozones
CONISS
Depth (cm)
0
50
100
150
200
250
300
350
400
450
500
550
600
650
700
750
1
2
500
1000
1500
20
20
1
5
10
50
100
150
10
20
Ed
Ec
Eb
Ea
D
C
B
200
400
600
Total sum of squares

Fig. S1

Supplementary material

Tephra analysis and interpretation

Methods

The chemical composition of single glass shards was determined on polished thin sections by electron-probe microanalyses to obtain major element data. Prior to the preparation of thin sections, samples were cleaned with 30 % H_2O_2 to remove organic matter and then dried with ethanol. Measurements were carried out using a CAMECA SX100 (WDS) instrument at the GFZ German Research Centre for Geosciences (Potsdam, Germany). Operating conditions were 15 kV accelerating voltage, 20 nA beam current, a defocused beam of 15 µm diameter and peak counting times of 20 s except for Na (10 s). For instrumental calibration, the Lipari obsidian was used as reference material (Hunt and Hill, 1996; Kuehn et al., 2011). Individual analyses of glass shards with total oxide sums <95 wt. % were excluded. Data of accepted analyses for individual tephra layers were recalculated to 100 wt. % and are given as mean values with 1σ standard deviation of n glass shards (Table S1). Petrological classification is based on the total-alkali-silica (TAS) diagram (Le Bas et al., 1986).

Results

The sediment record from Laguna Azul contains two macroscopic volcanic ashes (Figure S2). The lower tephra (AZU-T1 at 585.2 cm) is a white, fine-grained ash of 4–9 mm thickness with a maximum grain size of 150 µm. AZU-T1 mainly consists of colourless vitric glass shards of rhyolitic composition characterized by high silica (75.8 wt.%) and high potassium contents (4.0 wt.%; Table S1, Figure S4). The mineral assemblage comprises plagioclase, orthopyroxene, amphibole, biotite and Fe-Ti-oxide phenocrysts. The upper tephra layer (AZU-T2 at 581.9 cm) is also a vitric white ash of 7–9 mm thickness with a maximum grain size of 100 µm. The composition of glass shards is rhyolitic with a silica concentration similar to AZU-T1 (76.1 wt. %) but with a distinctly lower potassium content (1.8 wt. %) (Table S1). Its mineral assemblage comprises plagioclase, orthopyroxene, rare amphibole and Fe-Ti-oxide phenocrysts. The third light layer at 580 cm turned out to be a mixture of fine-grained lake sediments with reworked tephra from AZU-T1 and AZU-T2 (Figure S2). Radiocarbon dating of organic sediment between AZU-T1 and AZU-T2 at 583 cm yielded a 14C age of 5280 ±50 BP and a modelled age of 6090 cal. BP (Figure S2, Table 1).

Interpretation

The two tephra layers originate from different volcanic sources. Based on geochemistry of their glass shards (Figure S4, Table S1), AZU-T1 (modelled age: 6160 cal. BP) is attributed to an explosive eruption of the Northern Austral Volcanic Zone (NAVZ) located ~400 km NW of Laguna Azul. AZU-T2 (modelled age: 6050 cal. BP) is related to an eruption of Mt. Burney located ~260 km W of Laguna Azul.

A literature survey revealed that such a succession of tephra layers has not been reported. There are, however, individual volcanic ash deposits from other locations that chronologically compare with AZU-T1 or AZU-T2. AZU-T1 might be related to a 60 mm thick tephra documented at Vega Ñandú (for location of sites: Figure 1) radiocarbon-dated to 5700 -50/+140 cal. BP (Villa-Martínez and Moreno, 2007). The most likely candidate for correlation with AZU-T2 from Mt. Burney is a 1 mm thick tephra detected in the sediments of Lake Chandler dated to 5690 cal. BP (Kilian et al., 2003). Additional evidence for this tephra derives from an aeolian sequence near Lake Arturo. Here a 40 mm thick volcanic ash was deposited between two paleosols with bracketing ages of 6540 and 5550 cal. BP (Coronato et al., 2011). From Lake Ballena, a 35 mm thick Mt. Burney tephra was dated to 5440 -120/+140 cal. BP (Fontana and Bennett, 2012).

Analysis of biogenic silica

Biogenic silica (BSi) was analysed with the conventional automated leaching method (Müller and Schneider, 1993) and by applying a less time-consuming pressure pulping method with alkaline digestion in autoclaves. For both methods, BSi was subsequently detected by a continuous flow system with UV-VIS spectroscopy. The pressure pulping method yields better reproducibility with significantly lower standard deviations and has a higher throughput. This method, however, is applicable only to organic-rich sediments that are poor in minerogenic components, because siliciclastic components cause an overestimation of BSi values due to partial dissolution of silicates. Thus, for the lowermost part of the record (below 560 cm), where higher magnetic susceptibility points to clastic components, the conventional method was applied. For the pressure pulping method 3–5 mg of homogenized sample material were weighted into Teflon®-autoclaves. After addition of 20 ml 1 M NaOH, digestion was performed at 100 °C in a pressure pulping system for 2 or 4 h. The resulting solution was filtered, and an aliquot of 5 ml was diluted with 20 ml 1 M NaOH to determine BSi by UV-VIS spectroscopy. The residence time necessary for the pulping system was obtained by comparison with measurements of selected samples with the conventional method. In consequence, samples from the uppermost 200 cm were digested for 4 h, while a residence time of 2 h was applied for samples from 200–560 cm sediment depth. The amount of biogenic matter (BioM) is estimated as the sum of BSi and TOC, for the latter using the conversion factor of 2.13 (Dean, 1974).

Supplementary figures

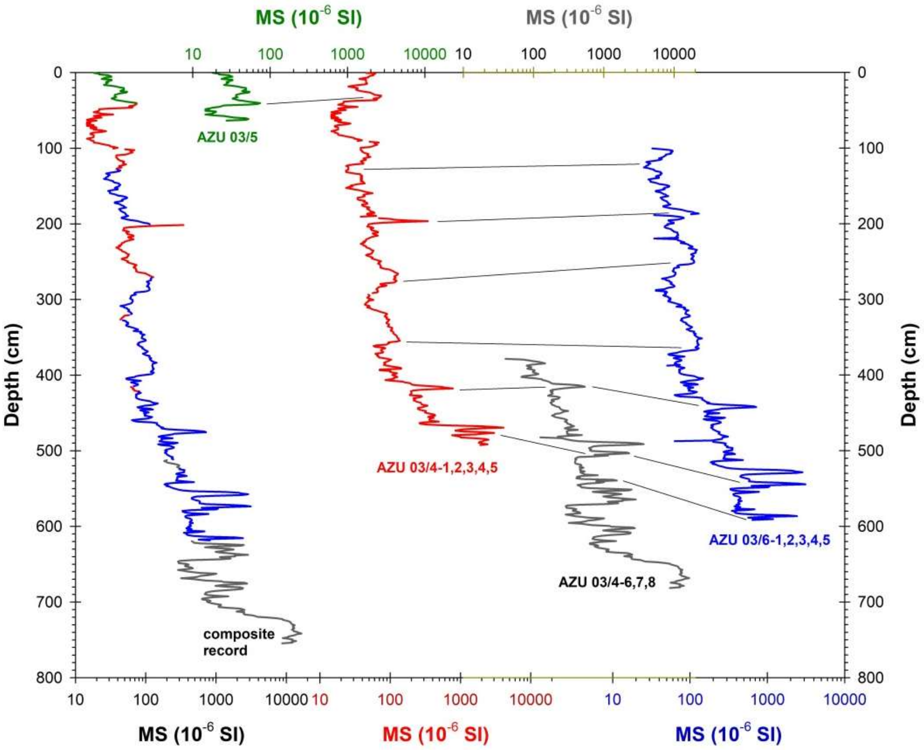

Figure S1: Composite record of magnetic susceptibility (MS) data as shown in Figure 2 (left). Furthermore, MS of gravity core AZU 03/5 (green) and of piston cores AZU 03/4 (red and grey) and AZU 03/6 (blue) are plotted vs depth. Correlations are marked by lines.

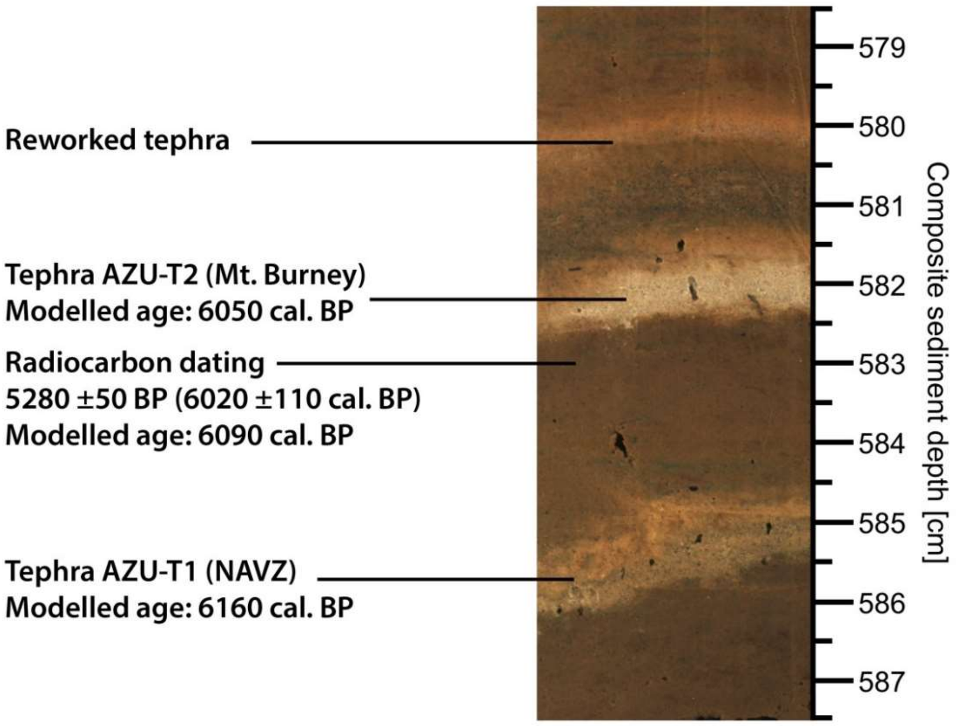

Figure S2: Photography of the core face between 587.5 and 578.5 cm sediment depth (lithological subunit Ea) with tephra layers AZU-T1 from the Northern Andean Volcanic Zone (NAVZ) and AZU-T2 from Mt. Burney with modelled ages. Additionally, the position of the radiocarbon age from 583 cm composite depth (Table 1) is indicated with radiocarbon as well as modelled ages.

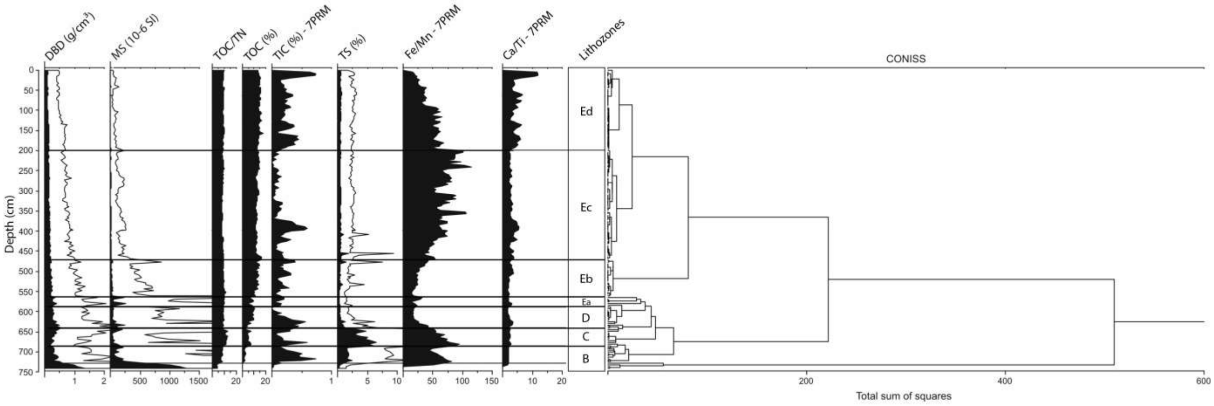

Figure S3: Results of unconstrained cluster analysis performed with eight representative organic and minerogenic sediment parameters: dry bulk density (DBD), magnetic susceptibility (MS), carbon to nitrogen ratio (TOC/TN), total organic carbon (TOC), total inorganic carbon (TIC) as a 7-point running mean (TIC7PRM), total sulphur (TS), iron to manganese ratio (Fe/Mn7PRM) and calcium to titanium ratio (Ca/Ti7PRM). Lithological units and subunits are labelled as A–Ed and indicated by horizontal lines.

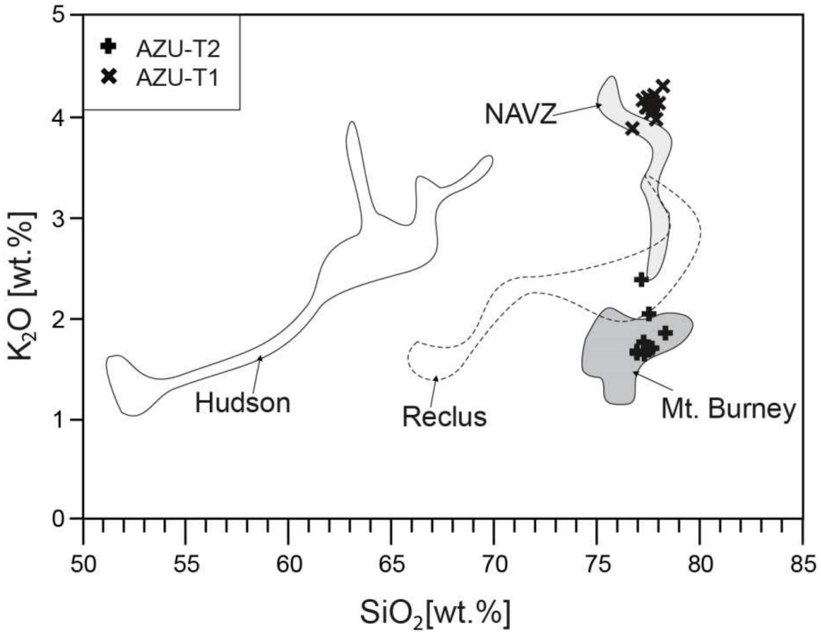

Figure S4: SiO2 vs K2O diagram assigns the two distal tephra layers from Laguna Azul (AZU-T1, AZU-T2) to their respective sources by comparison with other archives in southern Chile and Argentina (Bitschene and Fernandez, 1995; Haberzettl et al., 2007; Haberzettl et al., 2008; Kilian et al., 2003; Naranjo and Stern, 1998; Stern, 1990).

Supplementary tables

Table S1: Microanalytical electron-probe data (wt. %) of individual glass shards from two distal tephra layers documented in the Laguna Azul sediment record and of the Lipari obsidian standard.

Tephra sample	**SiO_2**	**TiO_2**	**Al_2O_3**	**FeO**	**MnO**	**MgO**	**CaO**	**Na_2O**	**K_2O**	**P_2O_5**	**Cl**	**Total**
AZU-T1	76.19	0.17	11.82	0.76	0.05	0.08	0.85	3.12	4.20	0.07	0.13	97.44
Sediment depth: 585.2 cm	76.64	0.14	12.60	0.88	0.02	0.15	1.02	3.27	4.06	0.00	0.20	98.98
Inferred age: 6160 cal. BP[a]	77.04	0.14	12.64	0.81	0.05	0.14	1.01	3.26	4.01	0.00	0.14	99.24
Source volcano: NAVZ[b]	75.99	0.13	12.19	0.96	0.00	0.16	0.98	2.99	4.12	0.02	0.17	97.71
	75.56	0.12	12.24	0.83	0.06	0.15	1.03	3.17	4.03	0.02	0.22	97.43
	75.99	0.15	12.97	0.88	0.07	0.13	1.24	3.61	3.85	0.01	0.16	99.06
	74.68	0.14	12.01	0.87	0.03	0.16	0.99	3.06	4.00	0.01	0.17	96.12
	74.03	0.13	11.87	0.89	0.02	0.16	1.00	3.28	4.01	0.03	0.15	95.57
	76.40	0.15	12.44	1.01	0.00	0.17	1.09	3.26	4.05	0.01	0.16	98.74
	75.67	0.12	12.10	0.93	0.00	0.19	0.96	3.17	3.87	0.03	0.14	97.18
	73.89	0.13	12.18	0.94	0.07	0.17	1.05	3.13	3.99	0.00	0.13	95.68
	76.96	0.12	12.44	0.87	0.03	0.17	0.95	3.28	4.07	0.00	0.17	99.06
	75.11	0.15	12.20	0.91	0.01	0.17	1.00	3.04	3.94	0.00	0.15	96.68
	76.92	0.11	12.20	0.85	0.03	0.16	0.93	3.16	4.08	0.02	0.16	98.62
Mean	**75.79**	**0.14**	**12.28**	**0.89**	**0.03**	**0.15**	**1.01**	**3.20**	**4.02**	**0.02**	**0.16**	**97.68**
std[c]	*1.04*	*0.02*	*0.31*	*0.06*	*0.03*	*0.03*	*0.09*	*0.15*	*0.09*	*0.02*	*0.03*	
AZU-T2	76.09	0.23	12.78	1.35	0.04	0.29	1.64	3.69	2.36	0.01	0.14	98.62
Sediment depth: 581.85 cm	76.79	0.17	12.45	1.15	0.03	0.26	1.45	3.75	1.82	0.04	0.15	98.06
Inferred age: 6050 cal. BP[a]	76.04	0.25	13.03	1.34	0.03	0.37	1.73	3.85	1.62	0.02	0.09	98.37
Source volcano: Mt. Burney	76.14	0.24	12.89	1.43	0.03	0.33	1.66	3.66	1.66	0.06	0.17	98.27
	76.10	0.26	13.08	1.32	0.04	0.29	1.83	4.21	1.64	0.00	0.15	98.92
	77.27	0.22	13.06	1.30	0.05	0.30	1.55	3.81	1.70	0.08	0.15	99.49
	73.74	0.25	12.77	1.20	0.08	0.26	1.76	4.01	1.61	0.06	0.10	95.84
	76.60	0.25	13.08	1.44	0.08	0.34	1.63	3.79	1.75	0.05	0.14	99.15
Mean	**76.10**	**0.23**	**12.89**	**1.32**	**0.05**	**0.31**	**1.66**	**3.85**	**1.77**	**0.04**	**0.14**	**98.34**
std[c]	*1.05*	*0.03*	*0.22*	*0.10*	*0.02*	*0.04*	*0.12*	*0.18*	*0.25*	*0.03*	*0.03*	
Lipari standard	74.69	0.05	13.34	1.56	0.07	0.04	0.70	3.84	4.72	0.07	0.36	99.44

[a] interpolated age according to age-depth model

[b] Northern Austral Volcanic Zone (volcanoes: Lautaro, Viedma, Aguilera)

[c] 1σ standard deviation

Table S2: Lithological units and subunits for the sediment record of Laguna Azul with corresponding depths and age ranges as well as arithmetic mean values for physical data (MS: magnetic susceptibility, WC: water content, DBD: dry bulk density), geochemical data (TC: total carbon, TN: total nitrogen, TS: total sulphur, TOC: total organic carbon, TOC/TN: organic carbon/nitrogen molar ratio, TIC: total inorganic carbon, BSi: biogenic silica), selected stable isotope (δ13C, δ15N), elements (Ti, Ca) and elemental ratios (K/Ti, Ca/Ti, Fe/Ti, Mn/Ti, Fe/Mn) as well as selected pollen (Poaceae, Nothofagus), absolute diatom abundance, sedimentation rate (SR), biogenic matter (BioM) and minerogenic matter (MM) (n.d. = not determined).

Litho-zone	**Depth range (cm)**	**Age range (cal. BP)**	**MS (10^{-6} SI)**	**WC (wt.%)**	**DBD (g/cm^3)**	**TC (%)**	**TN (%)**	**TS (%)**	**TOC (%)**	**TOC/TN**	**TIC (%)**	**BSi (%)**
Ed	0-201	-63-1310	39.39	88.18	0.11	14.69	1.84	0.51	14.40	9.13	0.29	52.04
Ec	201-466	1310-3000	81.39	84.29	0.15	12.65	1.70	0.51	12.51	8.58	0.15	47.84
Eb	466-563	3000-5410	260.06	78.88	0.21	12.46	1.53	0.43	12.28	9.38	0.19	35.92
Ea	563-588	5410-6240	1144.28	71.80	0.33	7.42	0.90	0.38	7.31	9.37	0.14	22.42
D	588-641	6240-8300	724.48	72.41	0.32	7.97	0.97	0.64	7.72	9.23	0.26	28.74
C	641-686	8300-10,100	919.90	71.19	0.31	5.69	0.57	4.48	5.46	11.10	0.25	25.73
B	686-728	10,100-11,790	1558.93	59.40	0.34	2.68	0.33	1.93	2.32	8.19	0.37	13.37
A	728-743	n.d.	10,843.71	24.36	1.12	0.23	0.05	0.47	0.19	4.24	0.05	1.30

Litho-zone	**Depth range (cm)**	**Age range (cal. BP)**	**$\delta^{13}C_{org}$ (‰)**	**$\delta^{15}N$ (‰)**	**Ti (cps)**	**Ca (cps)**	**K/Ti**	**Ca/Ti**	**Fe/Ti**	**Mn/Ti**	**Fe/Mn**
Ed	0-201	-63-1310	-25.75	4.16	35.10	162.75	0.16	5.03	21.58	0,62	45.53
Ec	201-466	1310-3000	-24.81	4.13	63.78	196.83	0.19	3.05	21.09	0,36	69.38
Eb	466-563	3000-5410	-25.96	5.13	95.72	220.96	0.31	2.44	44.07	1,91	26.25
Ea	563-588	5410-6240	-26.46	5.49	139.95	302.34	0.54	2.23	33.29	1,81	23.34
D	588-641	6240-8300	-27.71	5.69	148.48	327.79	0.33	2.22	48.73	2,63	23.45
C	641-686	8300-10,100	-31.16	5.90	96.82	220.45	0.36	2.37	113.74	1,56	69.73
B	686-728	10,100-11,790	-29.27	2.75	157.27	308.93	0.36	1.98	77.88	1,11	62.20
A	728-743	n.d.	n.d.	n.d.	283.37	494.27	0.33	1.75	30.52	0,51	56.34

Litho-zone	**Depth range (cm)**	**Age range (cal. BP)**	**Poaceae (%)**	**Nothofagus (%)**	**Absolute diatom abundance (10^6 valves/g)**	**SR (mm a^{-1})**	**BioM (%)**	**MM (%)**
Ed	0-201	-63-1310	56.56	37.49	31,531	2,33	82.69	14.27
Ec	201-466	1310-3000	58.06	34.63	2320	2,35	74.24	24.12
Eb	466-563	3000-5410	65.46	20.47	101	0,41	62.76	35.63
Ea	563-588	5410-6240	65.06	18.02	2	0,30	40.94	58.39
D	588-641	6240-8300	70.92	22.68	31	0,26	42.69	54.47
C	641-686	8300-10,100	68.65	33.14	1508	0,25	37.71	60.37
B	686-728	10,100-11,790	70.47	26.21	31	0,25	15.77	79.91
A	728-743	n.d.	n.d.	n.d.	n.d.	n.d.	1.58	98.39

Table S3: Mineralogical composition of selected samples from different lithological units of Laguna Azul based on XRD analysis.

Lithological unit or subunit	Depth (cm)	Age (cal. BP)	Detected minerals	Comments
Ec	391.5	2180	calcite	
Eb	474,5	3140	plagioclase	sandy layer S2
Ea	566.5	5530	plagioclase, quartz	sandy layer S1
D	619.5	7460	plagioclase, vivianite	
C	674.5	9660	pyrite, plagioclase	
B	719.5	11,470	quartz, pyrite (traces)	

References

Bitschene PR and Fernandez MI (1995) Volcanology and petrology of fallout ashes from the August 1991 eruption of the Hudson volcano (Patagonian Andes). In: Bitschene PR and Mendia J (eds) The August 1991 eruption of the Hudson volcano (Patagonian Andes): a thousand days after. Göttingen: Cuvillier, 27-54.

Coronato A, Fanning P, Salemme M, et al. (2011) Aeolian sequence and the archaeological record in the fuegian steppe, Argentina. Quaternary International 245: 122-135.

Fontana SL and Bennett KD. (2012) Postglacial vegetation dynamics of western Tierra del Fuego. The Holocene 22: 1337-1350.

Haberzettl T, Kück B, Wulf S, et al. (2008) Hydrological variability in southeastern Patagonia and explosive volcanic activity in the southern Andean Cordillera during Oxygen Isotope Stage 3 and the Holocene inferred from lake sediments of Laguna Potrok Aike, Argentina. Palaeogeography, Palaeoclimatology, Palaeoecology 259: 213-229.

Hunt JB and Hill PG (1996) An inter-laboratory comparison of the electron probe microanalysis of glass geochemistry. Quaternary International 34-36: 229-241.

Kilian R, Hohner M, Biester H, et al. (2003) Holocene peat and lake sediment tephra record from the southernmost Chilean Andes (53-55°S). Revista Geológica de Chile 30: 23-37.

Kuehn SC, Froese DG, Shane PAR, et al. (2011) The INTAV intercomparison of electron-beam microanalysis of glass by tephrochronology laboratories: Results and recommendations. Quaternary International 246: 19-47.

Le Bas MJ, Le Maitre RW, Streckeisen A, et al. (1986) A chemical classification of volcanic rocks based on the Total Alkali-Silica diagram. Journal of Petrology 27: 745-750.

Naranjo JA and Stern CR (1998) Holocene explosive activity of Hudson Volcano, southern Andes. Bulletin of Volcanology 59: 291-306.

Stern CR (1990) Tephrochronology of southernmost Patagonia. National Geographic Research 6: 110-126.

Villa-Martínez R and Moreno PI (2007) Pollen evidence for variations in the southern margin of the westerly winds in SW Patagonia over the last 12,600 years. Quaternary Research 68: 400-409.